Dust Lofting and Ingestion by Supercell Storms

ROBERT B. SEIGEL AND SUSAN C. VAN DEN HEEVER

Colorado State University, Fort Collins, Colorado

(Manuscript received 19 August 2011, in final form 28 December 2011)

ABSTRACT

Recent research pertaining to aerosol impacts on cloud microphysics has shown a need for understanding mineral dust entrainment into moist convection. The goal of this study is to examine the pathways in which nonmicrophysically active mineral dust is entrained into supercell storms within three commonly observed dust regimes. The Regional Atmospheric Modeling System (RAMS) with an interactive dust model that allows for surface emission was used to achieve this goal.

First, a supercell is simulated within an already dusty environment (EXP-BACKGROUND) to investigate ingestion purely from a background source. Second, the supercell is simulated within a clean background environment and lofts its own dust via the interactive dust model (EXP-STORM) to investigate the regime in which the only source of dust in the atmosphere is due to the storm itself. Finally, the supercell is simulated with a low-level convergence boundary introduced ahead of the supercell to investigate dust lofting by outflow boundary interactions (EXP-BOUNDARY). Results indicate that the supercell in EXP-BACKGROUND ingests large dust concentrations ahead of the rear flank downdraft (RFD) cold pool. Conversely, dust lofted by the cold pool in EXP-STORM is ingested by the supercell in relatively small amounts via a narrow corridor generated by turbulent mixing of the RFD cold pool and ambient air. The addition of a convergence boundary in EXP-BOUNDARY is found to act as an additional source of dust for the supercell. Results demonstrate the importance of an appropriate dust representation for numerical modeling.

1. Introduction

Dust is likely the most abundant aerosol species in the atmosphere, with global emission estimates ranging from 1000 to 3000 Tg yr^{-1} (Houghton et al. 2001). It can alter the atmosphere in a variety of complex manners. Climatologically, dust directly impacts the radiative budget through the absorption and scattering of both shortwave and longwave radiation (Quijano et al. 2000; Hansell et al. 2010). Additionally, dust indirectly affects the climate through aerosol indirect forcing that alters cloud properties and subsequent cloud radiative feedback effects (Twomey 1977; Albrecht 1989). On smaller scales, mineral dust can result in significant changes to the microphysical processes and associated precipitation rates of deep convective clouds by acting as cloud condensation nuclei (CCN) (Levin et al. 1996; Rosenfeld and Nirel 1996; Feingold et al. 1999; Ramanathan et al. 2001; DeMott et al. 2003; Rosenfeld et al. 2001; Yin et al. 2002; van den Heever et al. 2006, 2011; Khain et al. 2005, 2008; Twohy et al. 2009; Storer et al. 2010) and ice nuclei (IN) (Isono et al. 1959; Roberts and Hallett, 1968; Zuberi et al. 2002; DeMott et al. 2003; Sassen et al. 2003; Field et al. 2006; Möhler et al. 2006; van den Heever et al. 2006). While it is well known that mineral dust impacts cloud microphysics by acting as nuclei, our understanding of the manner in which mineral dust is ingested into deep convective storms is not well understood. This is due in part to the numerous types of dust events in our atmosphere and the poor representation of these different events in modeling experiments that investigate dust impacts on atmospheric processes.

While all mineral dust in the atmosphere initially comes from surface lofting by strong winds (Tegen and Fung 1994; Liu et al. 2007), the vertical distribution and concentrations of dust are different within specific meteorological events. First, the most prolific dust events occur due to large-scale dust lofting mechanisms, such as synoptic cyclones over deserts (Knippertz et al. 2007; Lewis et al. 2010), when mineral dust can be lofted higher than the boundary layer and transported over large distances. This mechanism can allow dust to behave as a well-mixed background aerosol. One example of this is

Corresponding author address: Robert B. Seigel, 1371 Campus Delivery Drive, Fort Collins, CO 80523.
E-mail: rseigel@atmos.colostate.edu

DOI: 10.1175/JAS-D-11-0222.1

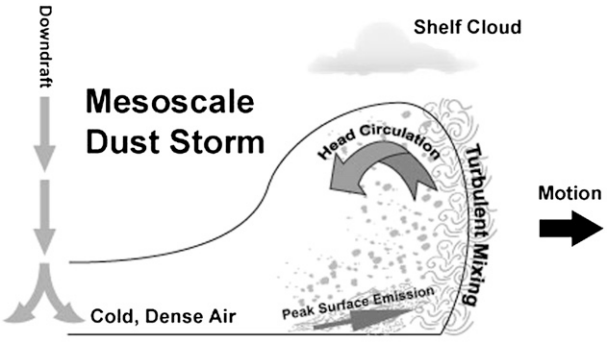

FIG. 1. Idealized schematic of a mesoscale convective dust storm. As negatively buoyant air from the downdraft collides with the surface, it spreads laterally and generates a density current. The strongest surface winds reside just behind the gust front where large concentrations of dust are present, providing the ''dust wall'' appearance seen in Fig. 2. Strong turbulent mixing at the gust front acts to detrain small amounts of dust from the cold pool air mass.

FIG. 2. Image of a strong dust storm that impacted Phoenix, Arizona, on 6 July 2011. This photo was taken from the National Weather Service Phoenix office in Tempe, Arizona, at 1945 MDT. [Source is http://www.wrh.noaa.gov/psr/pns/2011/July/DustStorm.php.]

the Saharan air layer (SAL), whereby a layer of Saharan dust has been found to affect convection as far west as the eastern United States (Prospero 1996, 1999; Perry et al. 1997; Sassen et al. 2003). The numerical representation of this dust regime, where dust is treated as a well-mixed background aerosol, is commonly used when studying dust impacts on convection (e.g., van den Heever et al. 2006, 2011; Zubler et al. 2011). A second commonly occurring dust regime occurs when convectively generated cold pools (Knippertz et al. 2009) loft large concentrations of dust that are localized, being contained behind the gust front (Fig. 1). These mesoscale dust storms, by which we mean the wall of dust within a cold pool (Fig. 2), are commonly referred to as haboobs (Sutton 1925; Lawson 1971) and occur within and beyond the reaches of the largest desert regions in the world. Within arid regions it has been found that these mesoscale dust storms can account for up to 30% of the regional dust mass budget (Miller et al. 2008). However, few dust studies truly represent the lofting of dust by the cold pool in order to understand its impacts on parent convection (Tulet et al. 2010). A third dust regime occurs when several discrete thunderstorms in a region produce their own boundaries and dust storms that all interact (Droegemeier and Wilhelmson 1985). In this regime, developing or mature convection could have access to multiple localized sources of dust. However, the pathways and the extent of dust ingestion by storms within this regime have not yet been examined. These various dust regimes demonstrate the complexities involved with correctly representing dust transport and ingestion in a numerical model.

Observational studies have found large concentrations of dust within convection (Levin et al. 1996; DeMott et al. 2003; Jensen et al. 2004; Twohy et al. 2009); however, collecting in situ dust ingestion data for these various regimes is extremely difficult and dangerous as high concentrations of dust damage plane engine turbines and clog air filtration systems (Miller et al. 2008). As a result, the method of obtaining a quantitative assessment of these data has typically been through numerical analyses (Takemi 2005; Tulet et al. 2010) using dust emission parameterizations that are shown to be accurate on the global scale (Kang et al. 2011). However, the grid spacing of global simulations make it difficult to resolve the small-scale circulations and sharp gradients associated with the cold pool that aid in dust lofting, transport, and subsequent ingestion by convection (Marsham et al. 2008; Reinfried et al. 2009). Therefore, precise ingestion pathways into the updraft of deep convective storms are still largely unknown.

The goal of this paper is therefore to gain a better understanding of the pathways by which dust is ingested by mesoscale storms within commonly observed dust regimes through the use of a high-resolution cloud-resolving model. To accomplish this goal, the Regional Atmospheric Modeling System (RAMS) (Pielke et al. 1992; Cotton et al. 2003; Saleeby and Cotton 2004) coupled with an interactive dust model (Smith 2007) is used to simulate a supercell thunderstorm within three commonly observed dust regimes. First, we simulate an idealized supercell within a horizontally homogeneous background dust profile to represent the ingestion of dust by a storm initiating within an already dusty atmosphere (e.g., the SAL, referred to as EXP-BACKGROUND). Second, we simulate the contribution and ingestion of mineral dust produced purely by the mechanics of the supercell itself (e.g., the haboob, referred to as EXP-STORM) by

utilizing a surface dust emission scheme and an initially dust-free background environment. Third, an independent surface convergence boundary is added to the domain ahead of the supercell to investigate dust ingestion resulting directly from the interaction between the supercell-produced gust front and the imposed convergence boundary (e.g., haboob interactions, referred to as EXP-BOUNDARY). These three model experiments represent a range of possible dust pathways into convection for commonly occurring dust regimes. The results of these experiments will aid future investigations into dust impacts on precipitation processes by demonstrating the sensitivities that differing dust sources have on ingested dust concentrations and locations.

The following section briefly describes the model used for these simulations with emphasis placed on pertinent schemes and the numerical setup for each experiment. Section 3 presents results from all three experiments, and section 4 provides discussion and conclusions of the results from each experiment. This paper is the first in a series of experiments dedicated to the understanding of mineral dust ingestion and its impact on the parent convection. The goal of this first paper is solely to understand the ingestion pathway of mineral dust into the lower region of a supercell within common dust regimes. Therefore, mineral dust in this experiment is not microphysically active. The remaining experiments in this series of papers will investigate the microphysical and radiative impacts of ingested dust on deep convection and will be reported on elsewhere.

2. Methods

a. Model description

The numerical model that was used for this study is the nonhydrostatic RAMS model (Pielke et al. 1992; Cotton et al. 2003; Saleeby and Cotton 2004), which uses a staggered Arakawa C grid. RAMS is appropriate for this numerical study because of its sophisticated microphysical, surface, and mineral dust parameterization schemes. The two-moment microphysical scheme (Meyers et al. 1997) predicts both mass mixing ratio and number concentrations of the hydrometeor species. The water species are categorized in eight forms: vapor, cloud droplets, rain, pristine ice, snow, aggregates, graupel, and hail (Walko et al. 1995). Within each category, the hydrometeors are assumed to conform to a generalized gamma distribution (Flatau et al. 1989; Verlinde et al. 1990). The bulk microphysical schemes within RAMS contain added sophistication by accessing previously generated lookup tables for the nucleation of aerosol species such as CCN, giant cloud condensation nuclei (GCCN), and ice nuclei (IN). The reader is referred to Saleeby and Cotton (2004) for a detailed description regarding the activation of CCN and GCCN, and to Meyers et al. (1997) regarding IN.

TABLE 1. Mass and size distribution for soil used in dust emission scheme. Following Tegen and Fung (1994).

	Size interval						
	1	2	3	4	5	6	7
Radius (μm)	0.15	0.265	0.471	0.831	1.5	2.65	4.71
Mass fraction	0.0009	0.0081	0.0234	0.0676	0.3	0.3	0.3

At the surface, RAMS divides each grid cell into a patchwork of water, bare soil, and vegetation over shaded soil that interacts with an online surface model, the Land Ecosystem-Atmosphere Feedback model (LEAF3) (Walko et al. 2000). For these experiments bare soil was chosen to represent 100% of each grid cell as we are examining dust storm development in arid regions.

Surface and soil studies have provided the information necessary to construct a model containing reliable surface dust emission, deposition and transport within RAMS that communicates online with LEAF3 (Smith 2007). Dust emission is diagnosed only when a surface wind velocity threshold value is reached and is a function of surface wind speed, soil type, and soil moisture (Marticorena and Bergametti 1995; Fécan et al. 1999). The wind threshold velocity for dust lofting is strongly dependent on particle diameter; therefore, the user must choose a soil size distribution to represent bare soil. For this experiment the soil distribution is based on Tegen and Fung (1994) and contains only silt and clay. The dust particle size distribution is partitioned into seven size increments, where sizes 1–4 represent clay and sizes 5–7 represent silt (Table 1). With respect to mass, silt constitutes 90% of the erodible materials, while clay is responsible for the remaining 10%. The partitioning of dust into multiple sizes allows for a more accurate representation of surface dust lofting.

If the wind speed at 10 m is greater than the computed wind threshold over moist soil U_{twet} and soil volumetric moisture content is less than 50% of saturation, then dust is allowed to be lofted from the surface. The amount of dust mass emitted from the surface is parameterized as a mass flux that is a function of 10-m wind speed and wind threshold velocity (Gillette and Passi 1988; Ginoux et al. 2001). From the mass flux, number concentrations for each particle size are computed using an assumed density of 2500 kg m^{-3} for clay and 2650 kg m^{-3} for silt (Tegen and Fung 1994). Finally, the concentrations for each clay size are summed up and added to the existing concentrations for clay species (referred to as the small dust mode), while the same procedure is performed for the silt species (referred to as the large dust mode). This

TABLE 2. RAMS configuration and options.

Model aspect	Setting
Grid	Arakawa C grid (Mesinger and Arakawa 1976)
	Single grid
	Horizontal grid: $\Delta x = \Delta y = 300$ m
	Vertical grid: Δz variable
	Δz (min) = 25 m
	Δz (stretch ratio) = 1.10 (10%)
	Δz (max) = 300 m
	Model top: ~22 km
	17 levels below 1 km AGL
Initialization	Horizontally homogeneous
	Idealized convective environment (Weisman and Klemp 1982)
	Idealized wind profile (Weisman and Klemp 1984)
Convective initiation	10 km wide, square bubble
	2 K thermal perturbation
	2 km depth
Time step	1 s
Simulation duration	3 h
Microphysics scheme	Two-moment bulk microphysics (Saleeby and Cotton 2004; Meyers et al. 1997)
	CCN background: 1600 cm^{-3}
	IN background: 10 000 kg^{-1}
Boundary conditions	Radiative lateral boundary (Klemp and Wilhelmson 1978a)
Turbulence scheme	Smagorinsky (1963) deformation K closure scheme with stability modifications by Lilly (1962) and Hill (1974)
Radiation scheme	Harrington (1997)
Surface scheme	LEAF3 (Walko et al. 2000)
Dust scheme	See section 2a

summation results in a single concentration for both the small and large dust mode. After lofting, the subsequent dust removal and transport schemes perform calculations with respect to these two modes. This results in a two-bin representation of dust within RAMS.

The removal mechanisms of each dust mode within the model include gravitational settling (Baron and Willeke 2001) and below-cloud scavenging by precipitation for all model levels below cloud base (Slinn 1982). The reader is referred to Smith (2007) for a more detailed summary of these parameterizations. Research is currently underway to develop parameterization schemes representing the scavenging and nucleation of mineral dust to form cloud droplets and ice crystals within cloud. As such, mineral dust in this experiment is not microphysically active and is simply used as an active tracer to investigate ingestion by supercell storms. As the goal of this paper is to investigate mineral dust ingestion into supercells, this should not significantly impact the results.

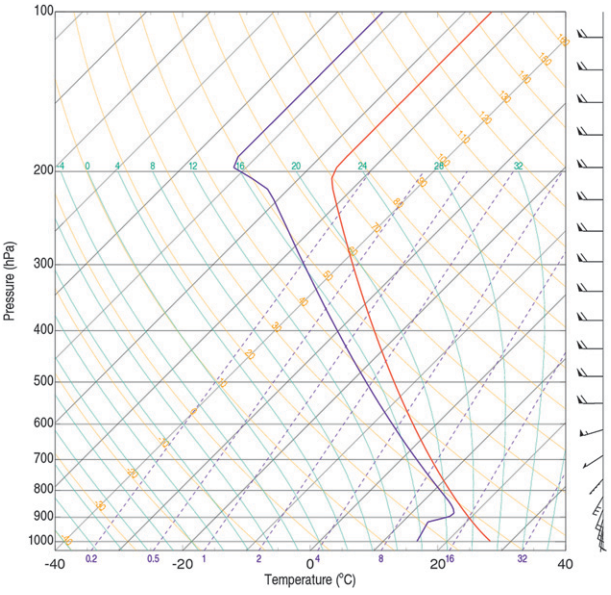

FIG. 3. Horizontally homogeneous environmental conditions initialized for all simulations. Red is the temperature profile and blue is the moisture profile. Following Weisman and Klemp (1982).

b. Experimental design

In this study, three idealized simulations are performed of a supercell to understand how mineral dust becomes entrained into such storms. To best resolve the cold pool and turbulent eddies responsible for dust lofting and transport, RAMS is configured as a high-resolution cloud-resolving model (CRM). Table 2 summarizes the model configuration for all simulations. The horizontal grid has a spacing of 300 m and the vertical grid spacing closest to the surface is 25 m and increases by 10% for each higher model level until a maximum of 300 m is reached, above which it stays at 300 m.

To initiate convection, a 10-km-wide, 2-km-deep warm bubble containing a uniform thermal perturbation of 2 K (Table 2) is used within a convective environment following Weisman and Klemp (1982) (Fig. 3). In addition to the thermodynamic profile, the veering wind profile favors the development of a right-moving supercell (Weisman and Klemp 1984). Supercell evolution within each experiment is identical. The following subsections briefly describe the dust regime used for each model experiment, the details of which are details are summarized in Table 3. For cloud and ice nucleation within all experiments, background concentrations of 1600 cm^{-3} and 10 000 kg^{-1} are used for aerosol species that can be activated as CCN and IN, respectively (Table 2). These aerosols are independent of the dust species.

TABLE 3. Mineral dust schemes used in each experiment.

Expt	Model initialized with background dust	Surface emission	Dry deposition	Below-cloud scavenging
EXP-BACKGROUND	✓	X	✓	✓
EXP-STORM	X	✓	✓	✓
EXP-BOUNDARY	X	✓	✓	✓

1) EXP-BACKGROUND

For this experiment, the surface dust emission parameterization is turned off and an initial horizontally homogeneous environmental profile of dust (Fig. 4) is used to represent the development of supercells within an already dusty environment. The vertical profile used to initialize the model consists of a surface concentration of 1000 cm^{-3} that linearly decreases to 20 cm^{-3} by 4 km AGL and is then held fixed at 20 cm^{-3} within the remainder of the domain. This vertical profile was chosen following observations documented by Chen and Fryrear (2002) of a midlatitude haboob in Big Spring, Texas. They measured a maximum concentration within 15 m of the surface of 1.3×10^3 $\mu g\ m^{-3}$ that, when using a mean particle diameter of 0.8 μm and a density of 2500 kg m^{-3} (small dust mode), produces a particle number concentration of ~1250 cm^{-3}. Surface dust emission is absent in this experiment; however, the remaining schemes within the dust model are still active, including dry deposition and below-cloud scavenging by precipitation.

2) EXP-STORM

To examine the contribution of ingested dust following lofting purely by the supercell itself, this simulation initially contains no background dust. The surface dust emission within the dust model is enabled. With no initial background dust (unlike EXP-BACKGROUND), all dust produced in this experiment originates from the surface. This provides a means to assess dust ingestion pathways into a supercell of that dust produced purely by the storm's own kinematics.

3) EXP-BOUNDARY

The aim of this experiment is to further our understanding of mineral dust ingestion as a direct result of outflow boundary interactions. The numerical setup of this experiment is identical to EXP-STORM (full dust model and no initial background dust) except that, 95 min after initialization, an independent surface convergence boundary is introduced ahead of the supercell outflow boundary. The addition of the surface convergence boundary at this time allows for 1) sufficient time for numerical stabilization of the boundary and 2) the interaction with the supercell outflow boundary during the analysis times of the other two experiments, thereby facilitating experiment comparisons. This additional convergence boundary will also contribute to lofted dust within the environment, thus making it potentially available for ingestion by the supercell, similar to what you might see in reality in an environment populated by numerous discrete storms. The convergence boundary is initialized by instantaneously inserting a north–south oriented −5-K thermal perturbation that is 1 km deep (surface to 1 km AGL) and positioned 20 km ahead of the approaching right-moving supercell. The cold, dense air generates two horizontally propagating outflow boundaries, one to the east and one to the west. The depth and temperature perturbation were chosen through trial and

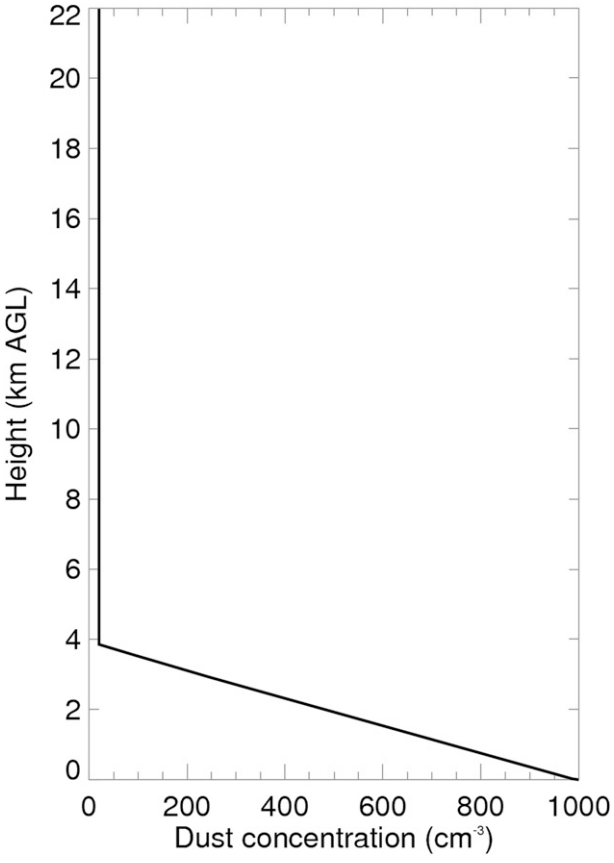

FIG. 4. Horizontally homogeneous dust profile (cm^{-3}) used for initialization of the EXP-BACKGROUND.

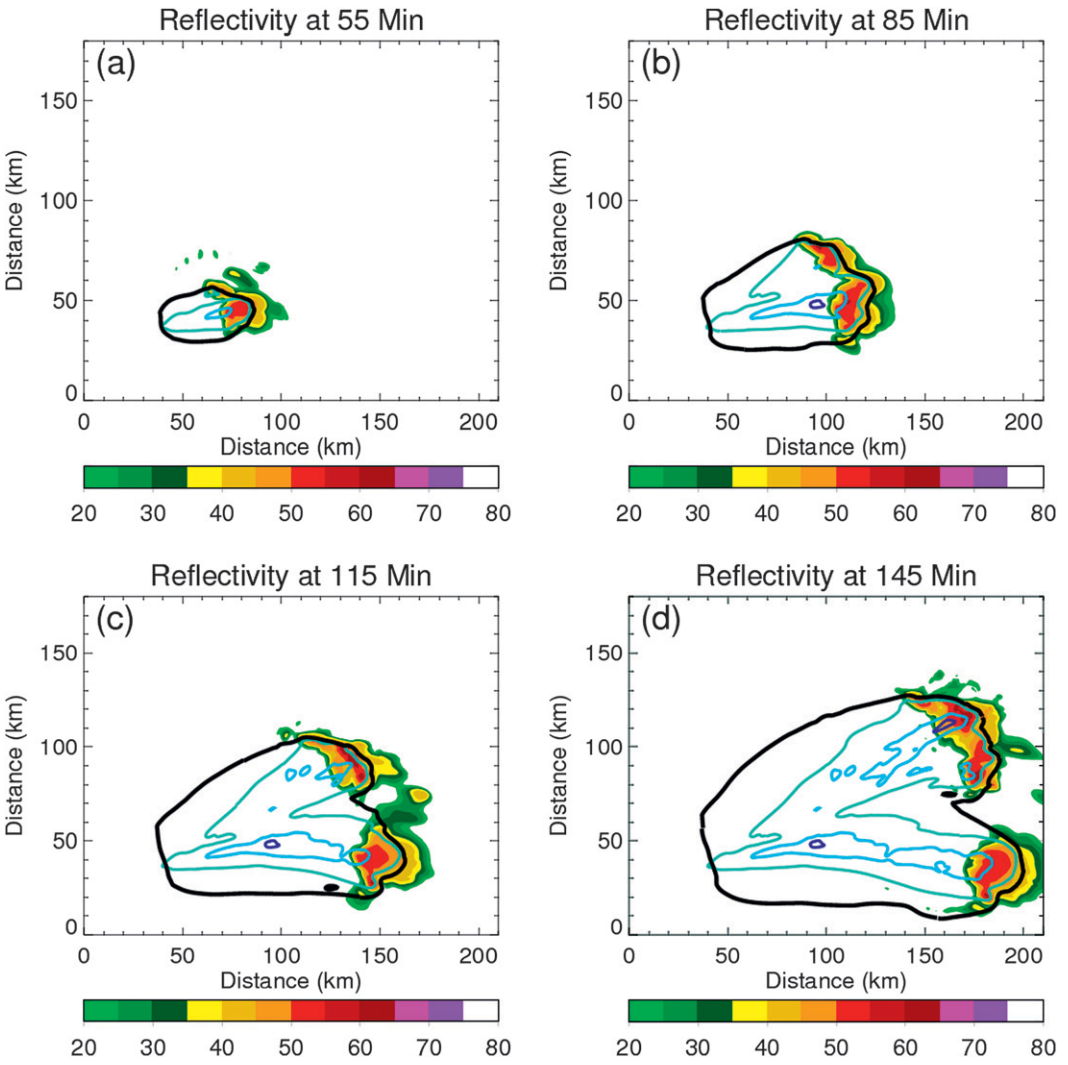

FIG. 5. Evolution of the splitting supercell. Model-derived reflectivity at 12 m AGL [shaded contours, following methodology of Matrosov (1999)], cold pool boundary [solid black contour, defined by -0.04 m^2 s^{-1} buoyancy following Tompkins (2001)], and total accumulated precipitation [1 mm (light blue), 10 mm (blue), and 20 mm (dark blue)] are shown at (a) 55, (b) 85, (c) 115, and (d) 145 min.

error in order to produce surface wind speeds and lofted dust concentrations similar to that produced by the supercell itself in EXP-STORM, thereby allowing for appropriate comparisons between experiments. The western outflow boundary of the convergence zone interacts with the supercell gust front and will be the focus of analysis. The following section first presents results pertaining to the supercell evolution for all three experiments and is followed by specific results from the three experiments just described.

3. Results

a. Supercell evolution and analysis

As mentioned in the previous section, a warm bubble is used to initiate convection. After 45 min the main updraft shows signs of splitting into a right and left mover (Klemp and Wilhelmson 1978b) due to the strong vertical wind shear of the environment (Weisman and Klemp 1982). To demonstrate the evolution of the split, Fig. 5 shows convection after 55, 85, 115, and 145 min into the simulation. To emphasize surface characteristics, the filled contours are model-emulated radar reflectivity at the lowest model level (~12 m AGL), which has been calculated following the methodology of Matrosov (1999). After 85 min the split can be seen in the surface reflectivity field with a clear separation in maximum dBZ. By 115 min, the right-moving supercell has taken on the appearance of a classic cyclonically rotating supercell (Weisman and Klemp 1984), where a hook is evident in both the reflectivity field and cold

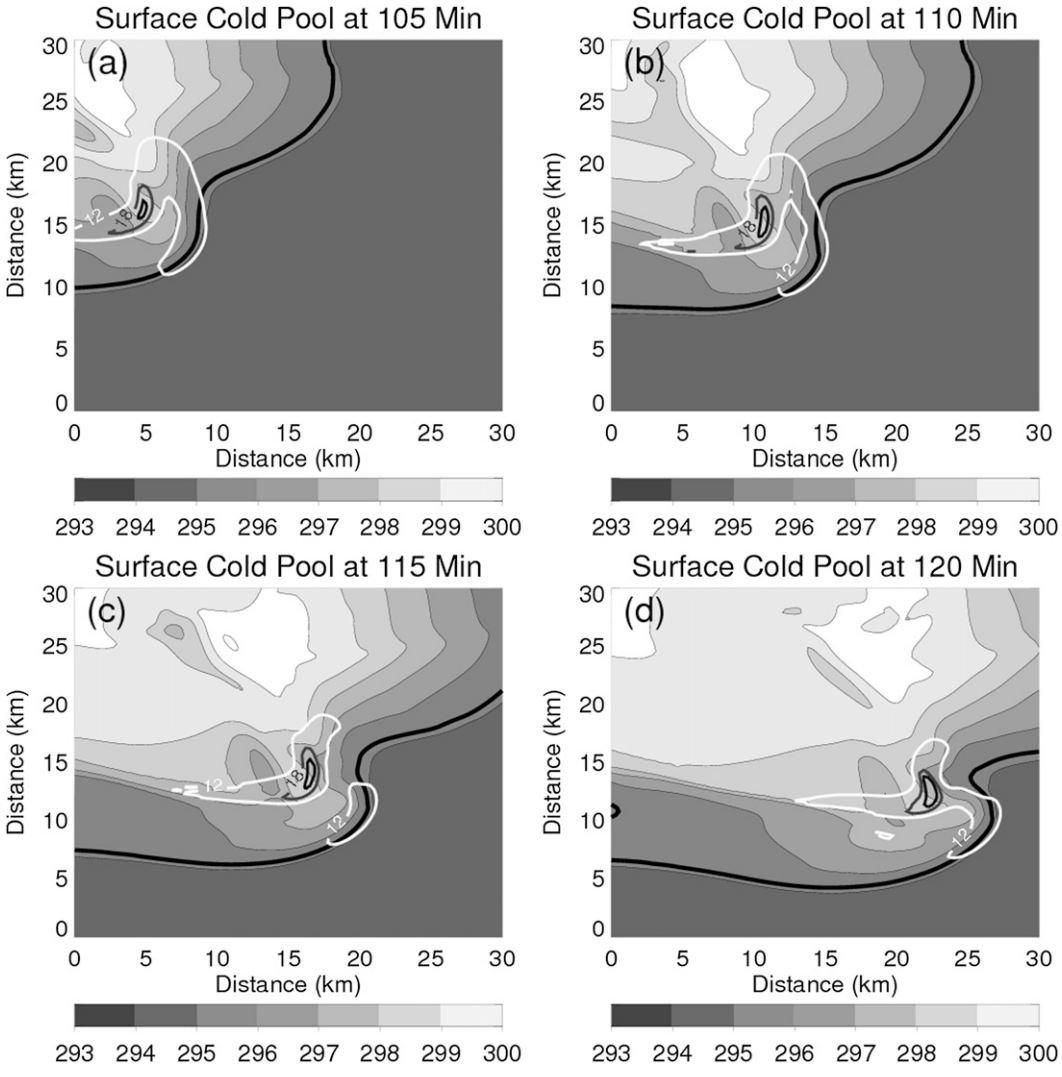

FIG. 6. Cold pool evolution of the right-moving supercell. Surface potential temperature (shaded contours), surface wind speed [12 (white contour), 18 (gray contour), and 22 m s^{-1} (dark gray contour)], and cold pool boundary (thick black contour) are shown at (a) 105, (b) 110, (c) 115, and (d) 120 min.

pool boundary on the southern flank of the storm. Thirty minutes later, the right mover is still well organized and is the dominant supercell owing to the veering wind profile imposed (Weisman and Klemp 1984). The path of the supercells can be seen via the accumulated surface precipitation (Fig. 5), where a right turn is evident in the southernmost cell. The cold pool boundary has been calculated following the methodology of Tompkins (2001) in which the cold pool is defined by air with -0.04 m^2 s^{-1} buoyancy relative to the domain averaged buoyancy at the desired model level. Because the right-moving supercell is the dominant cell simulated and the structure remained stable throughout the simulations, all analysis in this section is in regard to the right-moving supercell.

During analysis of the right-moving supercell, a 15-min period demonstrated strong cold pool forcing that generated a hook feature in the precipitation fields. Figures 6a–d show the cold pool (thick black contour) shape and characteristics during this time period after 105, 110, 115, and 120 min. It can be seen in Figs. 6a–d that after 120 min the southern portion of the cold pool pushes farther east than the cold pool region to the north as a result of being driven by a surge of air from the rear flank downdraft (RFD) (Markowski et al. 2002). This surge has reached the gust front and can be seen in the surface wind field (thin solid contours), whereby a small portion of >12 m s^{-1} winds have been pushed ahead of the main surface wind maximum. This local wind maximum along the RFD gust front is also

associated with a tongue of colder air (shaded contours) that aids in forcing the RFD gust front through baroclinic generation of horizontal vorticity (Markowski et al. 2003). The RFD surge seen in this 15-min period produces the hook shape in both cold pool and surface reflectivity that is a typical characteristic of a supercell. It is hypothesized that, when a hook signature is present, this is the most likely time period that tornadogenesis can take place as RFD-produced vorticity can be coupled with the supercell low-level mesocyclone (Markowski et al. 2008). This coupling aids in the collocation of the surface and cloud-base updrafts, which in turn would assist with dust ingestion. Thus, the time period from 105 to 120 min, which encompasses the development of the hook echo, will serve as the focus of this analysis.

Additionally, it is important to mention that dust analysis presented herein is with respect to the small dust mode. This mode has been chosen because analysis showed dust ingestion pathways between the small and large dust modes to be virtually the same. As the focus of this paper is on the ingestion pathways into the storm, presentation of both dust modes is redundant.

b. EXP-BACKGROUND

This experiment examines supercell development in a dusty environment with no contribution from surface lofting. To illustrate the three-dimensional nature of dust ingestion, Figs. 7 and 8 show various two-dimensional cross sections (at 105 and 120 min, respectively). Unless otherwise stated, all dust concentrations are shown as concentrations relative to background levels (i.e., the initial dust profile imposed), which provides a more representative assessment of ingestion.

Beginning at the surface Fig. 7a shows a plan view of the mineral dust distribution, cold pool boundary, and wind flow associated with the right-moving supercell. It can be seen that within the RFD cold pool, the dust concentrations are significantly lower than the low-level ambient concentrations of dust. This is due to the advection of less dusty air from aloft to the surface by the storm downdraft. As the RFD transports less dusty air, the surface wind spreads this ''cleaner'' air mass throughout the cold pool, while the remainder of the surface air contains near background levels of dust.

Moving higher aloft toward cloud base, which is located around 1800 m AGL, Fig. 7b shows a plan view at 2 km AGL illustrating the dust distribution and upward and downward fluxes associated with the updraft and downdraft of the supercell, respectively. The dust concentration and dust flux fields together demonstrate dust ingestion near cloud base. The positive flux values in conjunction with elevated dust concentrations illustrate the region of maximum dust ingestion, whereby updraft air is advecting higher concentrations of dust from below cloud base into the storm. Conversely, regions of large negative fluxes depict the region of the storm that is transporting dust from within the storm to lower levels. It can be seen that the area of largest positive vertical flux at 2 km AGL occurs ahead of the maximum dust concentration at this level, while the largest negative vertical flux occurs behind the maximum concentration. This signature shows the motion and ingestion of the supercell: as the supercell propagates eastward, the updraft atop the surface cold pool raises the dust concentration (shown by large fluxes) and shifts the dust distribution and concentration maximum farther east.

To further illustrate the flow regime and ingestion within the region of largest dust concentrations, Fig. 7c shows an east–west vertical cross section through the 2-km-AGL maximum dust concentration. From this figure it can be seen that a large region of elevated dust concentrations exists; however, the largest elevated dust concentrations at any vertical level still remain within the updraft while the lowest elevated concentrations are confined to the downdraft. The upward vertical motion ahead of the cold pool and just below cloud base (i.e., the main updraft) is occurring where large elevated dust concentrations are present. This indicates that the transport of dust into the parent storm in this case occurs due to the updraft within the top of the boundary layer where vertical motion and high dust concentrations are collocated.

To isolate the contributions of dust ingestion due to the horizontal and vertical components of the wind, Fig. 7d shows upward dust flux in the shaded contours and horizontal dust flux in vector form, where the length of the vector indicates the magnitude of the horizontal dust flux (maximum value is $\sim 14\ \mathrm{cm}^{-2}\ \mathrm{s}^{-1}$) and the vector direction indicates flux direction in the x–y plane through the cross-sectional surface. To best isolate dust ingestion into the storm, which is the primary focus of this experiment, the flux values within the cold pool and associated with the downdraft are removed from the figure for this analysis. The vertical cross-section location, cold pool boundary, and condensate boundary in Fig. 7d are the same region as in Fig. 7c. Within the main updraft, dust is fluxed both vertically and northwestward. Conversely, within the backside of the updraft and the downdraft dust is being advected from the east and northeast, respectively. This cyclonic turning of the advective motion is in agreement with the typical cyclonic circulation of right-moving supercells (Weisman and Klemp 1982). As previously mentioned, the majority of the dust ingestion in this experiment after 105 min occurs out ahead of the cold pool from the upper portion of the boundary layer into the updraft. This is reinforced quantitatively in Fig. 7d by the relative values of upward dust flux and

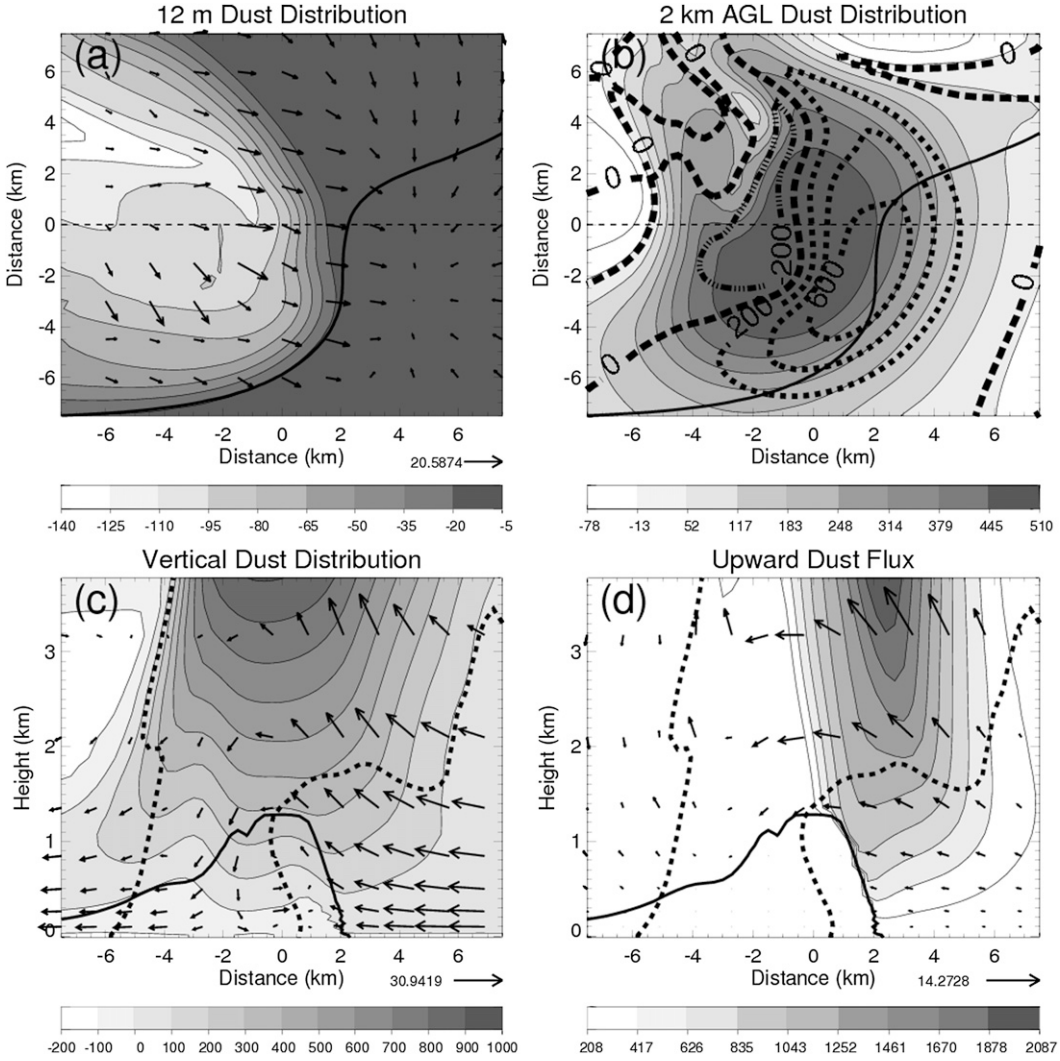

FIG. 7. EXP-BACKGROUND at 105 min. (a) Surface dust concentration (cm^{-3}) relative to the initialized background profile (shaded contours), surface cold pool boundary (solid black contour), surface wind vectors, and cross section location (thin dashed black line) in (c). (b) The 2-km AGL dust concentration (cm^{-3}) relative to the initialized background profile (shaded contours), surface cold pool boundary (solid black contour), vertical dust flux through the 2-km AGL surface (thick dashed line denotes the zero line; thin dashed lines denote positive fluxes; dash-dot lines denote negative fluxes in 10^3 cm^{-2} s^{-1} intervals), and cross section location (thin dashed black line) in (d). (c) Vertical cross section at the location shown in (a) with dust concentration (cm^{-3}) relative to the initialized background profile (shaded contours), cold pool boundary (solid black contour), 0.5 g kg^{-1} total condensate (dotted contour), and storm-relative winds parallel to cross section plane. (d) As in (c), but with upward dust flux (shaded contours; 10^3 cm^{-2} s^{-1}; downward dust flux not depicted), cold pool boundary (solid black contour), 0.5 g kg^{-1} total condensate (dotted contour), and horizontal dust flux through cross section plane (vectors; 10^3 cm^{-2} s^{-1}).

horizontal dust flux. The large spatial coverage of upward dust flux into cloud base is collocated with the updraft of the storm, similar as in Fig. 7c, and has values on the order of 1000×10^3 cm^{-2} s^{-1}. Conversely, horizontal dust flux, which can be related to lateral entrainment, has maximum values on the order of 10×10^3 cm^{-2} s^{-1} near the center of the updraft and decreases toward cloud boundary. The two orders of magnitude difference between the vertical and horizontal dust flux shows that dust ingestion is mainly driven by the vertical component of the wind (i.e., the updraft).

Figure 8 is identical to Fig. 7, but for 120 min into the simulation, which is the time at which the RFD gust front has strongly pushed ahead of the northern gust front in a hook shape, as described earlier. When comparing the two figures, the magnitudes and characteristics of the

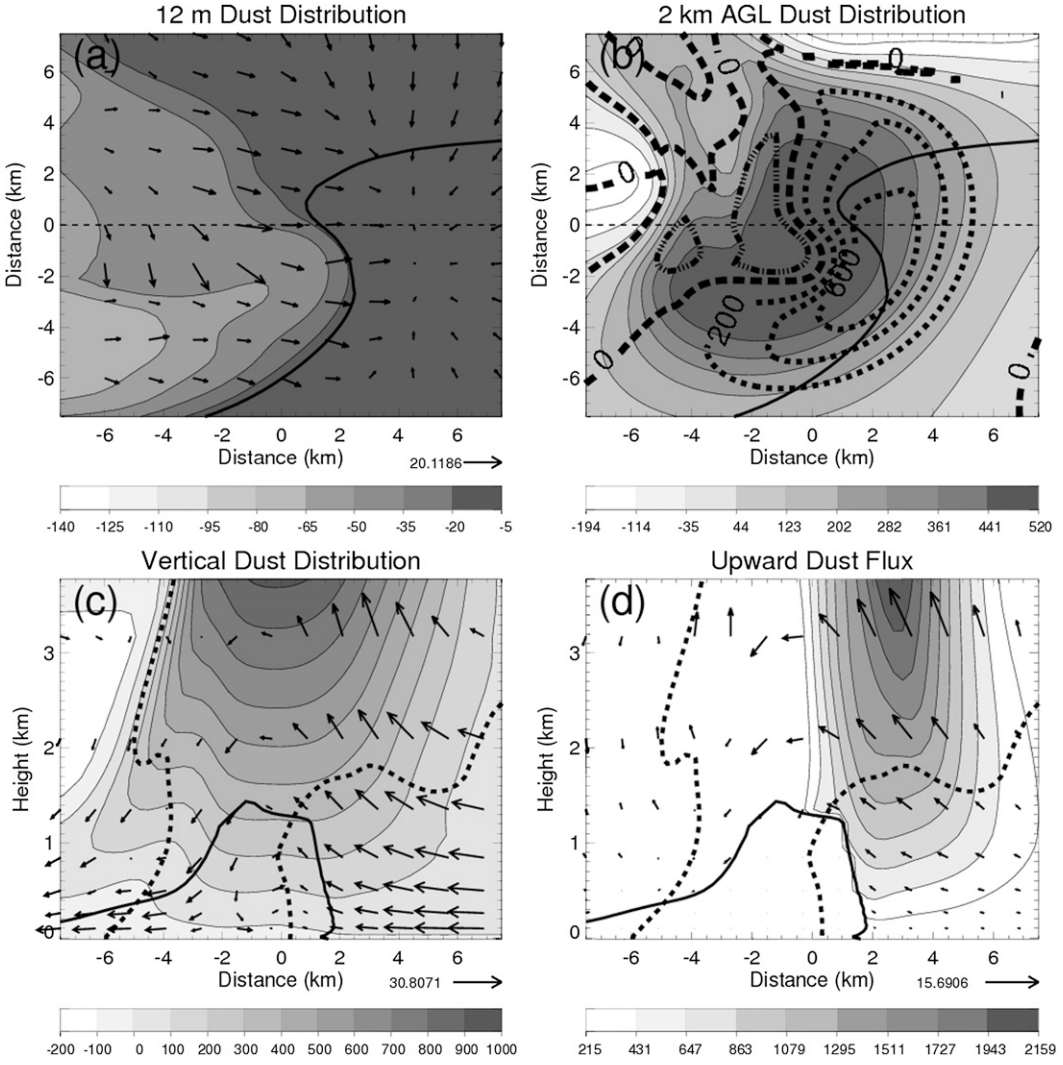

FIG. 8. As in Fig. 7, but at 120 min.

quantities plotted are virtually the same, indicating that, even after strong cold pool forcing has occurred, dust ingestion into the updraft remains virtually the same. While the storm updraft strength within the boundary layer may be dependent on the cold pool, this 15-min period indicates that ingestion of background dust by the supercell is somewhat independent of the cold pool forcing, as long as the updraft has access to the dusty environmental air near the top of the boundary layer out ahead of the storm.

To more precisely identify dust ingestion into supercells from a dusty atmosphere, Fig. 9 shows parcel trajectories into the supercell during this 15-min period. These offline parcel trajectories are calculated using model data with a temporal resolution of 1 min that are spatially and temporally interpolated to 10 m and 1 s to allow for more precise trajectories. The trajectory calculations are performed following the resolved flow fields and do not include the effects of dust sedimentation, which is a reasonable assumption for vertical speeds associated with supercells. Figures 9a and 9b show parcel initialization at 105 min relative to the surface and the dashed vertical plane (depicted in Fig. 9a), respectively. After hundreds of parcel releases, 20 parcels most representative of both cold pool and environmental air at different heights AGL are shown in their respective horizontal and vertical locations (Figs. 9a,b). After 15 min of trajectory analysis, the final locations of the 20 parcels are shown in Figs. 9c and 9d relative to the horizontal and vertical planes. The parcels that were ingested deep into the updraft were initially located ahead of the cold pool and well above the surface, thereby confirming the dust ingestion pathway of environmental dust by the supercell from the top

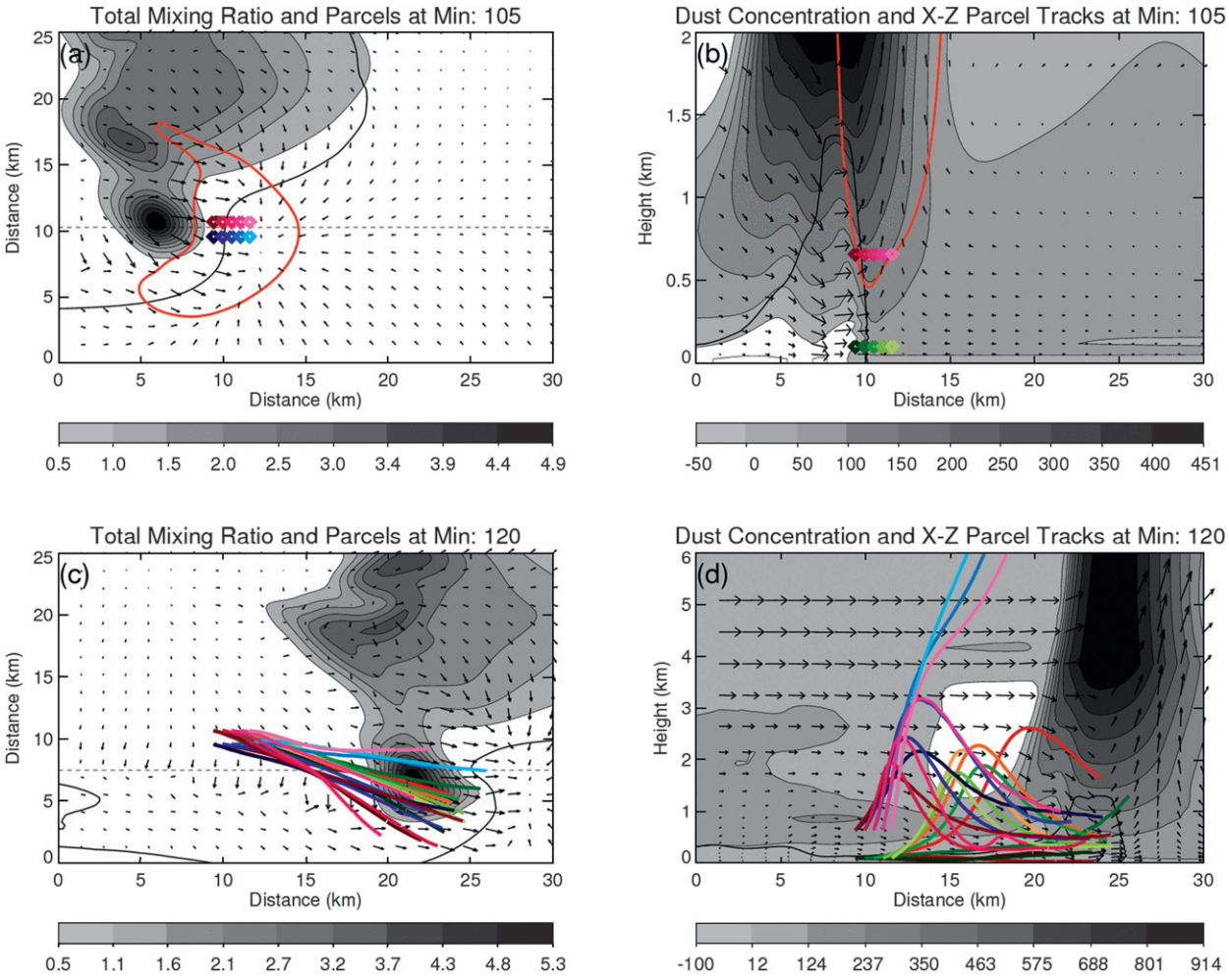

FIG. 9. EXP-BACKGROUND parcel trajectories during the 15-min period from 105 to 120 min. (a) At 105 min, total mixing ratio (shaded contours), surface cold pool boundary (solid black contour), surface wind vectors, 2 km AGL 5 m s^{-1} updraft (red solid contour), and initialized parcel locations in the horizontal plane. Although hidden, five additional green parcels lie beneath the pink parcels and five additional orange parcels lie beneath the blue parcels. (b) At 105 min, dust concentration (cm^{-3}) relative to the initialized background profile (shaded contours), cold pool boundary (solid black contour), wind vectors parallel to vertical plane, 5 m s^{-1} updraft (solid red contour), and initialized parcel locations in the vertical plane. (c) At 120 min, total mixing ratio (shaded contours), surface cold pool boundary (solid black contour), surface wind vectors, and final parcel locations in the horizontal plane. (d) At 120 min, dust concentration (cm^{-3}) relative to the initialized background profile (shaded contours), cold pool boundary (solid black contour), wind vectors parallel to vertical plane, and final parcel locations in the vertical plane. For (c) and (d), parcel motions are from left to right.

of the boundary layer ahead of the cold pool and into the updraft.

c. *EXP-STORM*

The purpose of the second experiment is to examine the ingestion of dust lofted purely by the supercell itself. This is achieved by modeling the storm within an initially dust-free environment and making use of the dust emission scheme to allow for the lofting of dust by the winds within the cold pool. Figures 10 and 11 show the same plots (at 105 and 120 min) as in Figs. 7 and 8.

At 105 min into the simulation the surface distribution of dust (Fig. 10a) is closely linked to that of the surface winds (maximum plotted vector is ~21 m s^{-1}), as dust lofting is strongly dependent on the 10-m wind speed. The strong surface winds that are generated by the RFD loft and transport the mineral dust within the RFD cold pool, distributing the dust both horizontally (Fig. 10a) and vertically (Fig. 10c). As shown in Fig. 10a, the range of maximum lofted dust concentrations are ~1100–1700 cm^{-3}, which is relatively consistent with haboob observations from Chen and Fryrear (2002), who measured 15-m-AGL dust concentrations of

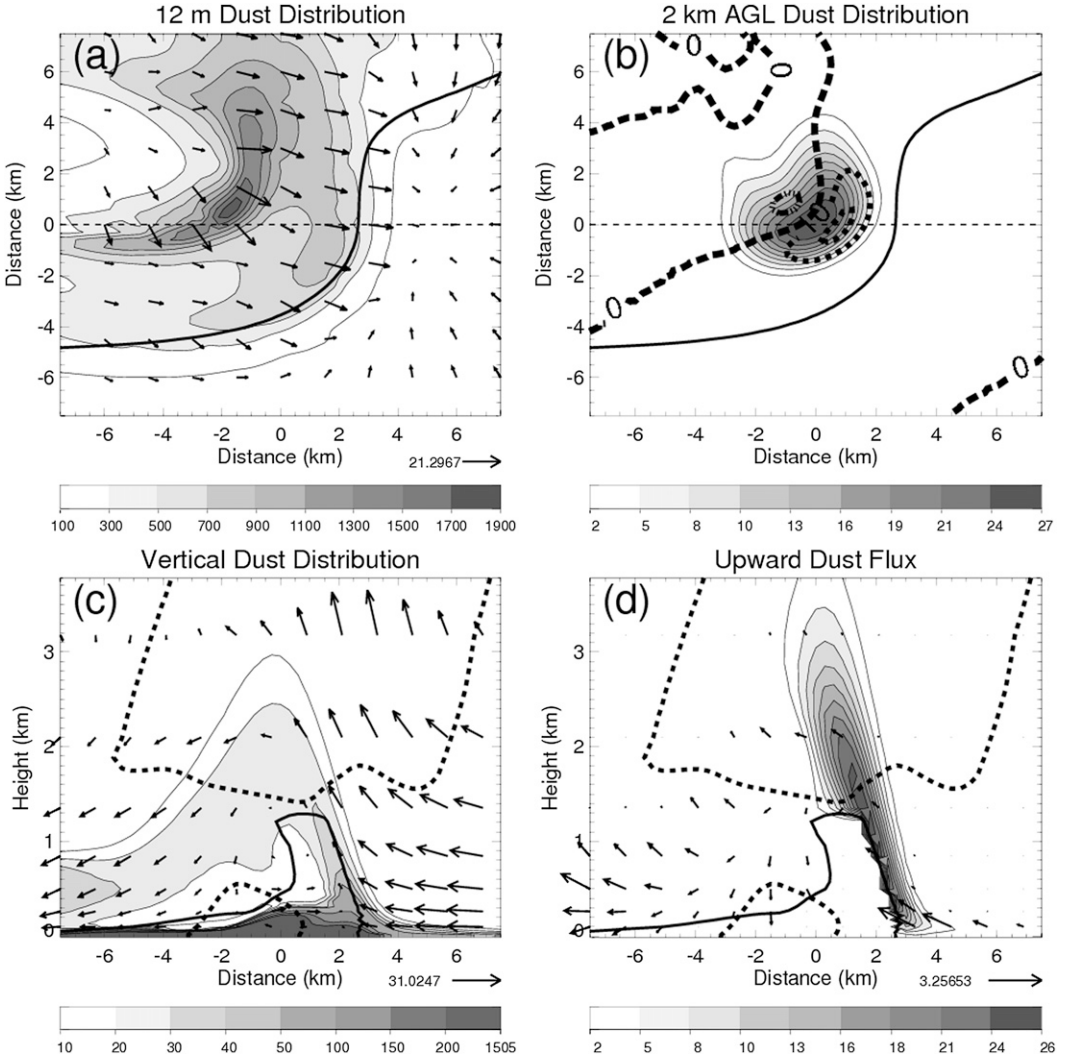

FIG. 10. EXP-STORM at 105 min. All plots are identical to Fig. 7. Note that the last contour interval of dust concentration in (c) is from 200 cm^{-3} through the maximum value, as a small number of grid cells exhibit concentrations of this magnitude.

$\sim$1250 cm^{-3}. Although the maximum simulated surface dust concentrations are larger than the haboob observations, it is to be expected given that the supercell simulated in this experiment produced surface winds in excess of 20 m s^{-1} while the haboob only produced a maximum surface wind of 14 m s^{-1}.

As the dusty cold pool propagates within the ambient air, turbulent mixing at the leading edge of the RFD cold pool allows the dusty air to become mixed with the unstable environmental air (Fig. 1) and associated low-level updraft (as will be seen later in this section). The dusty air at the leading edge of the RFD cold pool is detrained from the cold pool and forced into the rearward portion of the main updraft of the supercell. This produces a 2-km-AGL maximum dust concentration of $\sim$30 cm^{-3} (Fig. 10b) from a pathway closely tied to the RFD gust front (Fig. 10d). Even though the cold pool in EXP-STORM produces surface dust concentrations larger than the maximum background concentration in EXP-BACKGROUND, significantly lower concentrations are ingested into the updraft of EXP-STORM ($\sim$30 cm^{-3}) compared with that in EXP-BACKGROUND ($\sim$500 cm^{-3}). Additionally, the horizontal spatial extent of the vertical dust flux (Fig. 10d) is very narrow in comparison with EXP-BACKGROUND (Figs. 7d and 8d). The large differences in both magnitude and spatial extent of ingested dust between EXP-STORM and EXP-BACKGROUND demonstrates how difficult it is for a supercell to ingest dust produced by its own cold pool as opposed to dust that is available from the

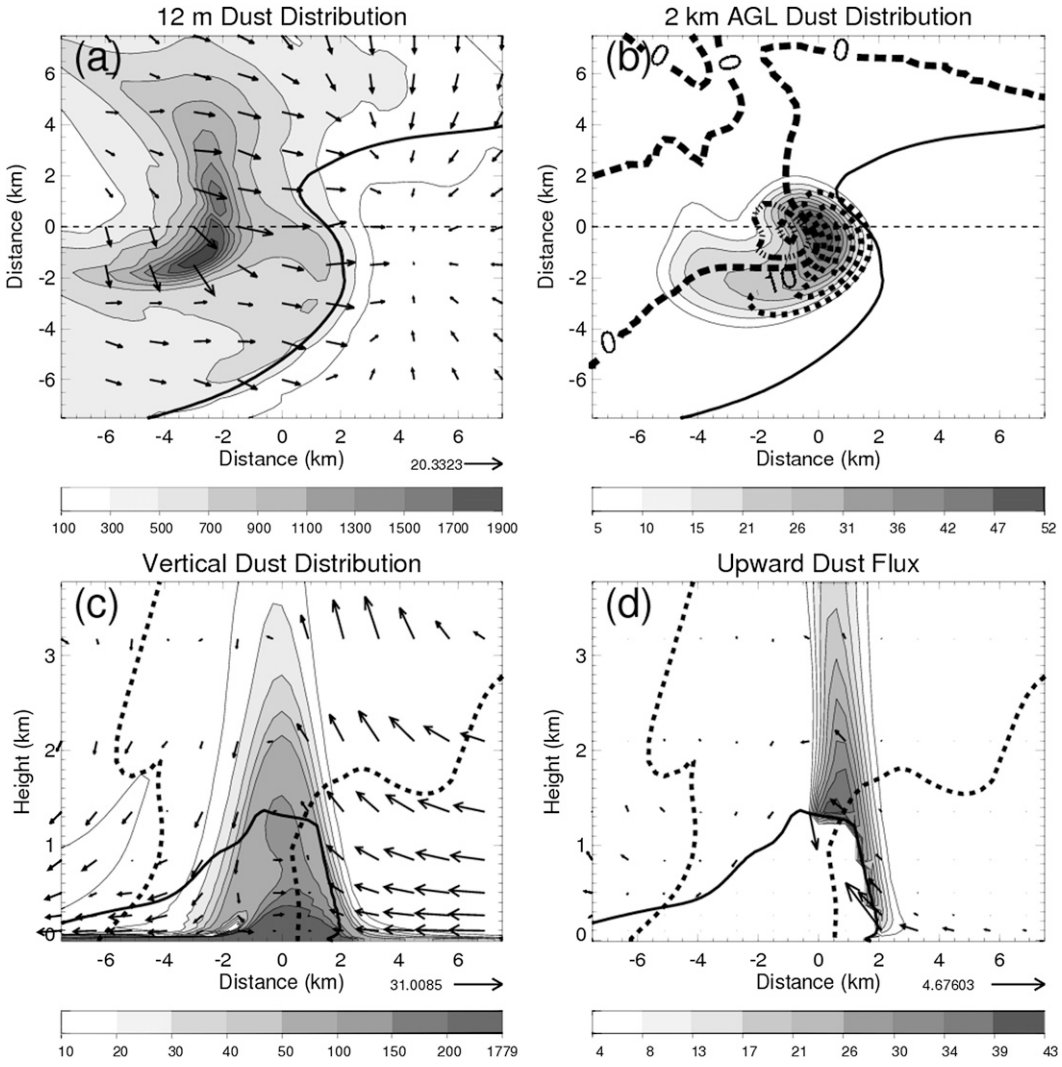

FIG. 11. As in Fig. 10, but at 120 min.

ambient environment. While haboobs are associated with large concentrations of dust kicked up within the cold pool, the majority of this dust may not make it into the parent storm's updraft.

After 120 min of simulation time (Fig. 11) the dust ingestion pathway has shifted farther north as a result of the RFD surge that generated the hook echo. As the RFD winds surged further east relative to the forward flank downdraft (FFD), the low-level winds formed a vertically stacked circulation (note the more upright distribution of upward dust flux in Fig. 11d vs Fig. 10d) beneath the 2-km-AGL maximum dust concentration that closely resembles the location of classical supercell tornadogenesis (Lemon and Doswell 1979; Markowski et al. 2002; Lerach et al. 2008; Snook and Xue 2008). This new region, which is still closely tied to the gust front (Fig. 11d), advects approximately two times more dust into the updraft as compared with 15 min earlier (Fig. 10) and contains much larger vertical fluxes. Similar to EXP-BACKGROUND, the relative contributions of horizontal (values near cloud base are $\sim 1 \times 10^3$ cm^{-2} s^{-1}) and vertical dust fluxes (values near cloud base are $\sim 30 \times 10^3$ cm^{-2} s^{-1}) to dust ingestion show that dust ingestion is dominated by the vertical wind. While the horizontal location of maximum dust ingestion changes between 105 and 120 min, the dependency on the RFD cold pool boundary remains consistent, and ingestion into the rearward portion of the updraft occurs at the cold pool and ambient air interface. Although the dust concentrations ingested by the supercell have doubled by this time, they remain an order of magnitude smaller than the dust concentrations ingested by EXP-BACKGROUND, thus further demonstrating the difficulty for cold pool–produced dust to become ingested by the parent supercell.

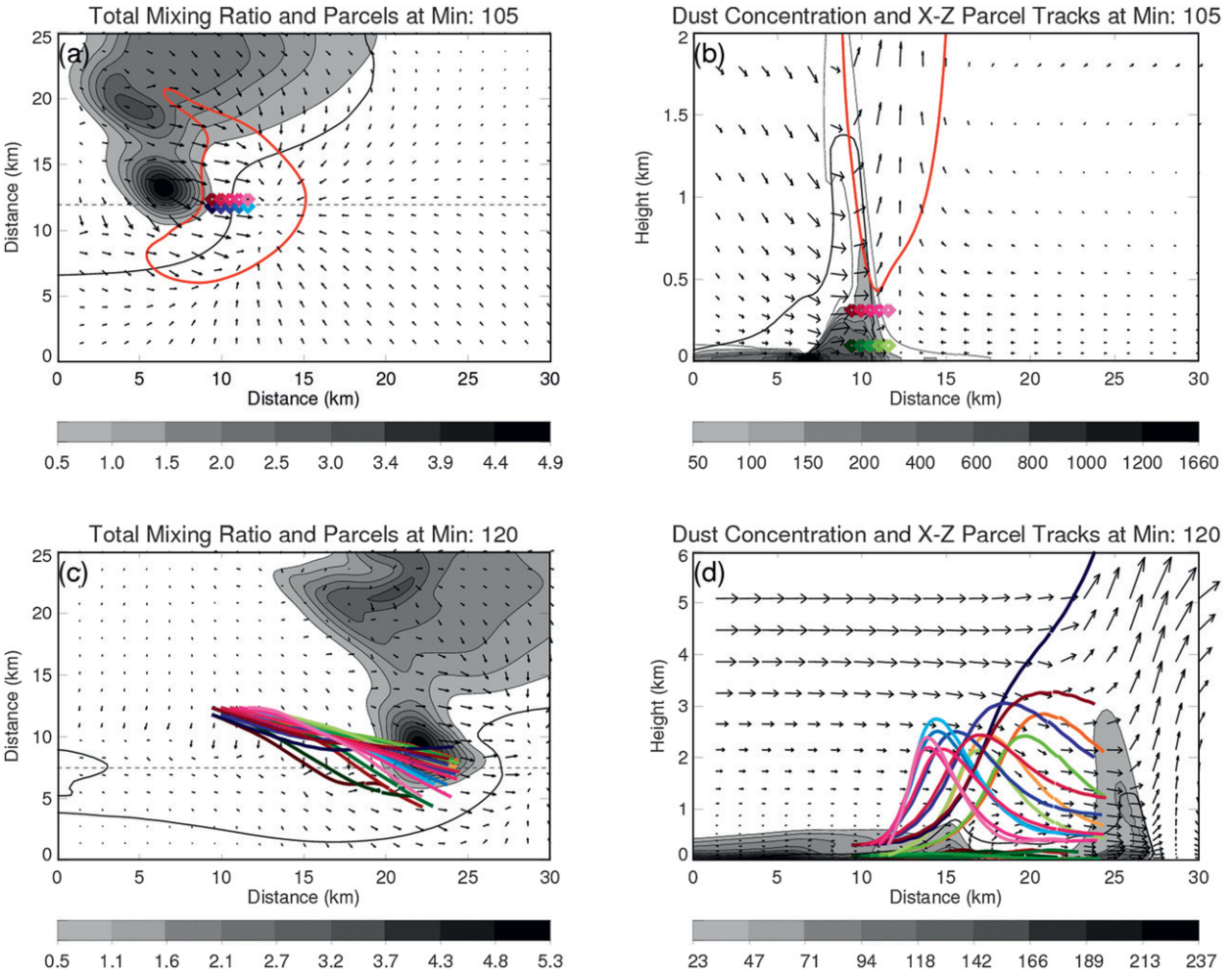

FIG. 12. EXP-STORM with parcel trajectories during the 15-min period from 105 to 120 min. Plots are as in Fig. 9.

To more precisely identify dust ingestion pathways into supercells from dust originating at the surface within the cold pool, Fig. 12 shows parcel trajectories into the supercell during this 15-min period. Similar to Fig. 9, Figs. 12a and 12b show the 20 parcels that best represent the transport processes occurring in the cold pool and at the gust front where dust is present. The parcels are initialized at 105 min relative to the horizontal and the vertical plane using the same methodology for EXP-BACKGROUND trajectory analysis. The final locations of the 20 parcels are shown in Figs. 12c and 12d relative to the horizontal and vertical planes, respectively.

Results from this trajectory analysis coincide with results shown in Figs. 10 and 11. The only parcel to be ingested by the supercell and transported higher than 4 km AGL originated from within the cold pool, as shown by the 300-m-AGL darkest blue parcel, confirming the cold pool origin of ingested dust by the supercell. At the start of the 15-min trajectory analysis, the ingested parcel was located near the RFD surge (shown by large wind vectors within cold pool of Figs. 12a and 12b) where increased convergence was occurring. The increased convergence (not shown) enhanced the turbulent mixing along its pathway, thereby allowing detrainment of this parcel from the cold pool into the updraft where it is subsequently ingested by the supercell. For EXP-STORM, these trajectories confirm the aforementioned results that dust ingested by the supercell originates within the RFD cold pool winds and is detrained at the gust front surface, resulting in entrainment within the rearward portion of the updraft.

d. EXP-BOUNDARY

To further study the ingestion of dust by supercell storms within common dust regimes, the third experiment aims to investigate the influence of an additional surface convergence boundary on dust ingestion. This is an important experiment because several supercells or deep convective

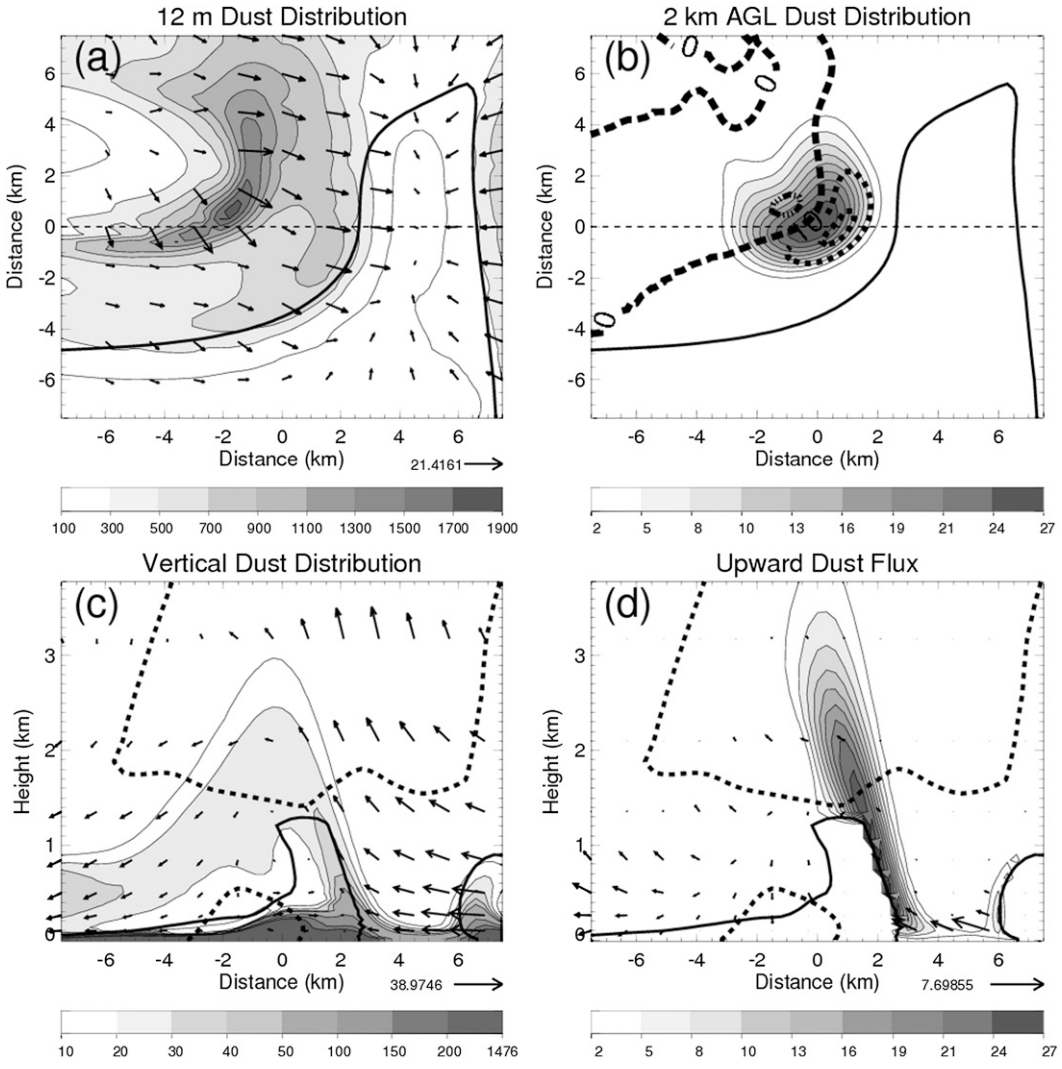

FIG. 13. EXP-BOUNDARY at 105 min. Plots are as in Fig. 10.

storms commonly form within the same environment, resulting in numerous boundary collisions (Bluestein and Weisman 2000). Figures 13, 14, and 15 show plots similar to those in Figs. 10 and 11 but because the boundary interaction takes place relatively quickly, the times presented are at 105, 107, and 109 min into the simulation, respectively.

Ten minutes after the boundary initialization (Fig. 13) the surface boundary can be seen to the east of the supercell cold pool. The convergence boundary has surface dust lofting (Figs. 13a,c) comparable to the leading edge of the RFD gust front, with maximum values of ~700 cm^{-3}. Additionally, the convergence boundary is advecting dust into the boundary layer air ahead of the supercell, both horizontally and vertically (Fig. 13d). As the boundary collides with the supercell gust front at 107 min (Fig. 14), interaction can be seen first near the surface, where the distribution of dust within the supercell cold pool and the convergence boundary cold pool appear to merge (Fig. 14c). While dust is being ingested in a similar fashion to EXP-STORM via the supercell RFD cold pool, dust can also be seen beginning to enter the supercell near cloud base farther ahead of the RFD cold pool (Figs. 14b,d), providing an additional dust ingestion pathway into the supercell at this time. As the convergence boundary lofts dust into the boundary layer air ahead of the supercell, the supercell updraft begins to ingest the dusty environmental air through a similar pathway as EXP-BACKGROUND. Two minutes later (Fig. 15), full boundary interaction has taken place and the 2-km-AGL concentration values have doubled due to the combination of boundary- and supercell-forced ingestion. Vertical advection of dust has also increased both in magnitude and height AGL because

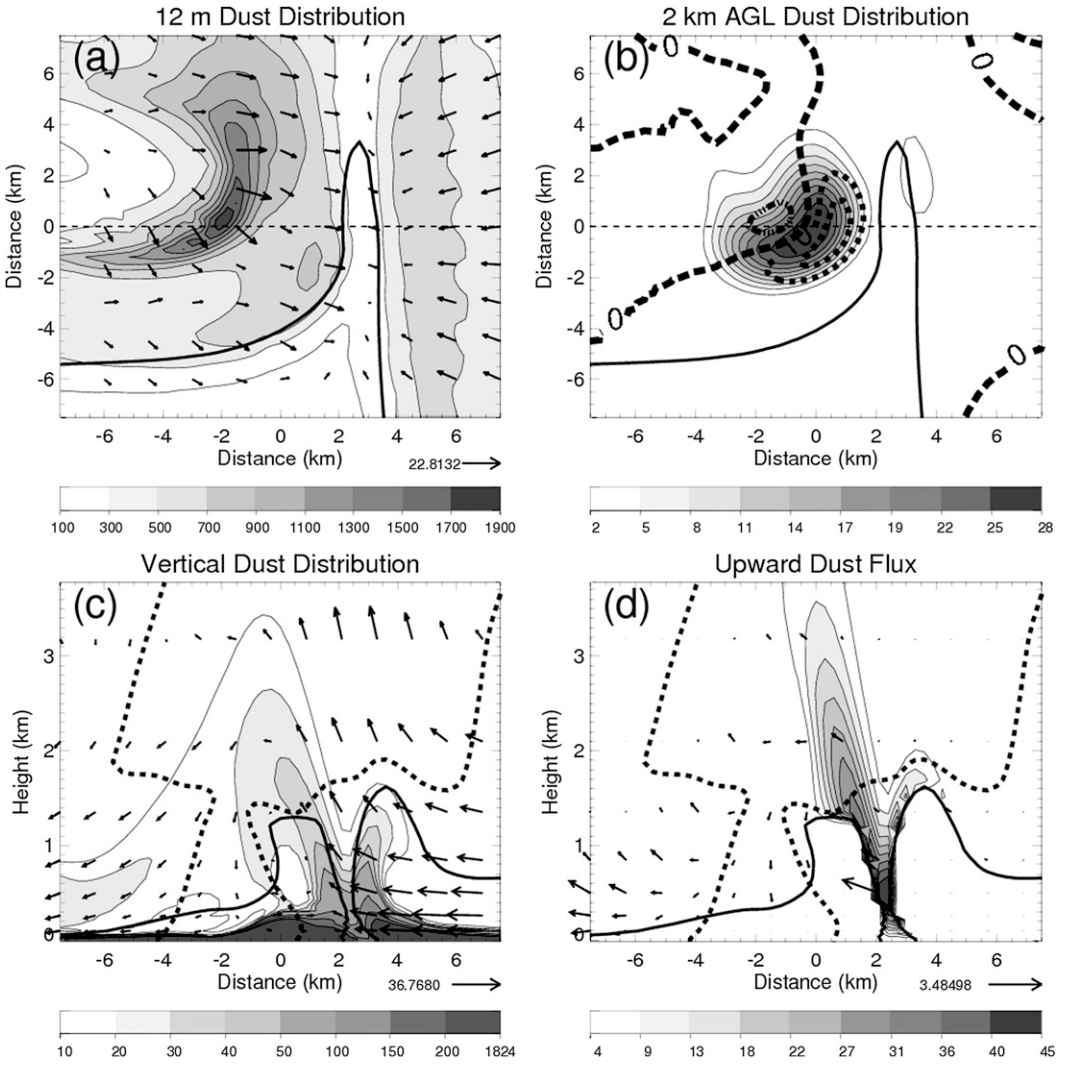

FIG. 14. As in Fig. 13, but at 107 min.

of 1) increased concentrations of dust due to the combination of RFD and convergence boundary–produced dust and 2) the enhanced updraft as a result of the boundary collision (Droegemeier and Wilhelmson 1985). The plume of mineral dust that has been ingested into the main updraft of the supercell as a result of the boundary interaction can be seen in Fig. 15c where a ''tower'' of >50 cm^{-3} is present. After this time (109 min), the supercell propagates over the cooler and more stable air in the wake of the convergence boundary and this leads to weakening and eventual dissipation of the supercell.

Using the same analysis as previously, parcel trajectories for this simulation are shown in Fig. 16. In general, the parcels that were ingested into the main updraft of the supercell as a result of the boundary collision originated primarily from the ambient air (dark red and dark blue parcels in Figs. 16c,d). As shown with Figs. 13–15, dust lofted by the imposed convergence boundary is advected into the ambient air through westward and vertical advection at the gust front. This advected dust is then ingested into the supercell updraft prior to the arrival of the supercell cold pool. These trajectories (Fig. 16) confirm the aforementioned results of this experiment that for this environmental regime dust ingested into the supercell is enhanced by dust within the ambient air ahead of the supercell cold pool that is generated by the convergence boundary.

4. Discussion and conclusions

The overall goal of this experiment is to gain a better understanding of mineral dust ingestion pathways into severe convective storms. The three simulations performed in this experiment were designed to emulate

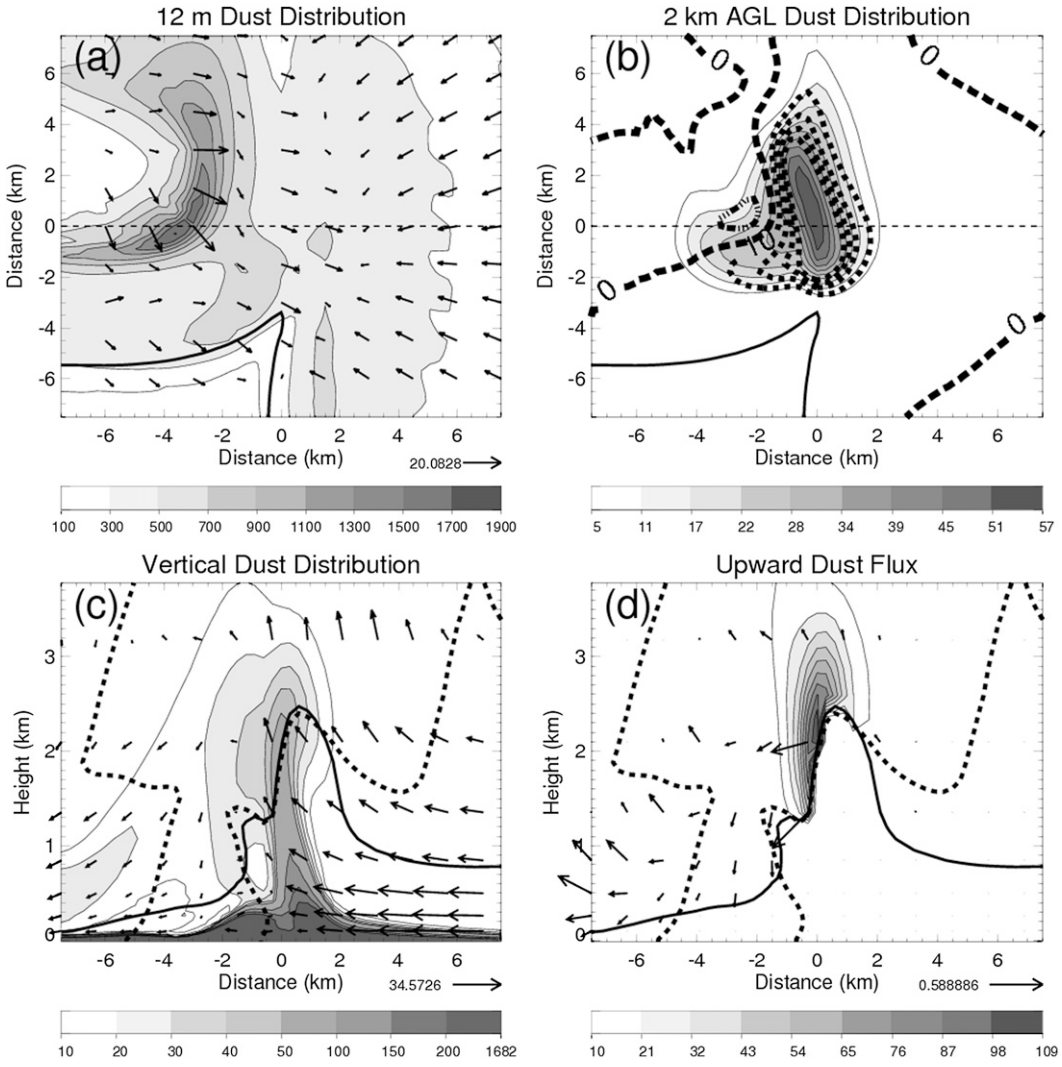

FIG. 15. As in Fig. 13, but at 109 min.

some of the more common environmental regimes that provide a source of dust for ingestion by supercell storms. The first simulation, EXP-BACKGROUND, investigated a regime in which a supercell develops in an already dusty atmosphere in order to examine dust ingestion by the supercell solely from the environment. Conversely, EXP-STORM explored the regime in which a supercell develops in a dust-free environment and the only dust available for ingestion is generated by the supercell itself. Finally, EXP-BOUNDARY investigated dust ingestion pathways within the regime of a convergence boundary interacting with a supercell whereby both phenomena loft their own dust within an initially clean environment. The three dust regimes simulated in this experiment provide a range of possible dust pathways into convective storms and represent common dust environments observed in reality and utilized in numerical investigations.

The results of the three simulations demonstrate substantial differences in the location and quantity of dust ingested by the supercell. If the only source of dust is within the environmental air (i.e., EXP-BACKGROUND), then relatively large amounts of dust originating from the upper region of the boundary layer ahead of the cold pool are ingested predominantly by the vertical component of the supercell updraft. Conversely, if the atmosphere is originally void of mineral dust and the only dust lofted into the atmosphere is due to the kinematics of the supercell cold pool (i.e., EXP-STORM), then relatively small concentrations are ingested by the supercell via a very narrow region at the edge of the RFD cold pool. Dusty cold pool air is detrained at the interface between the cold pool and the ambient air and then entrained into the rearward portion of the updraft just ahead of the gust front. When investigating the influence

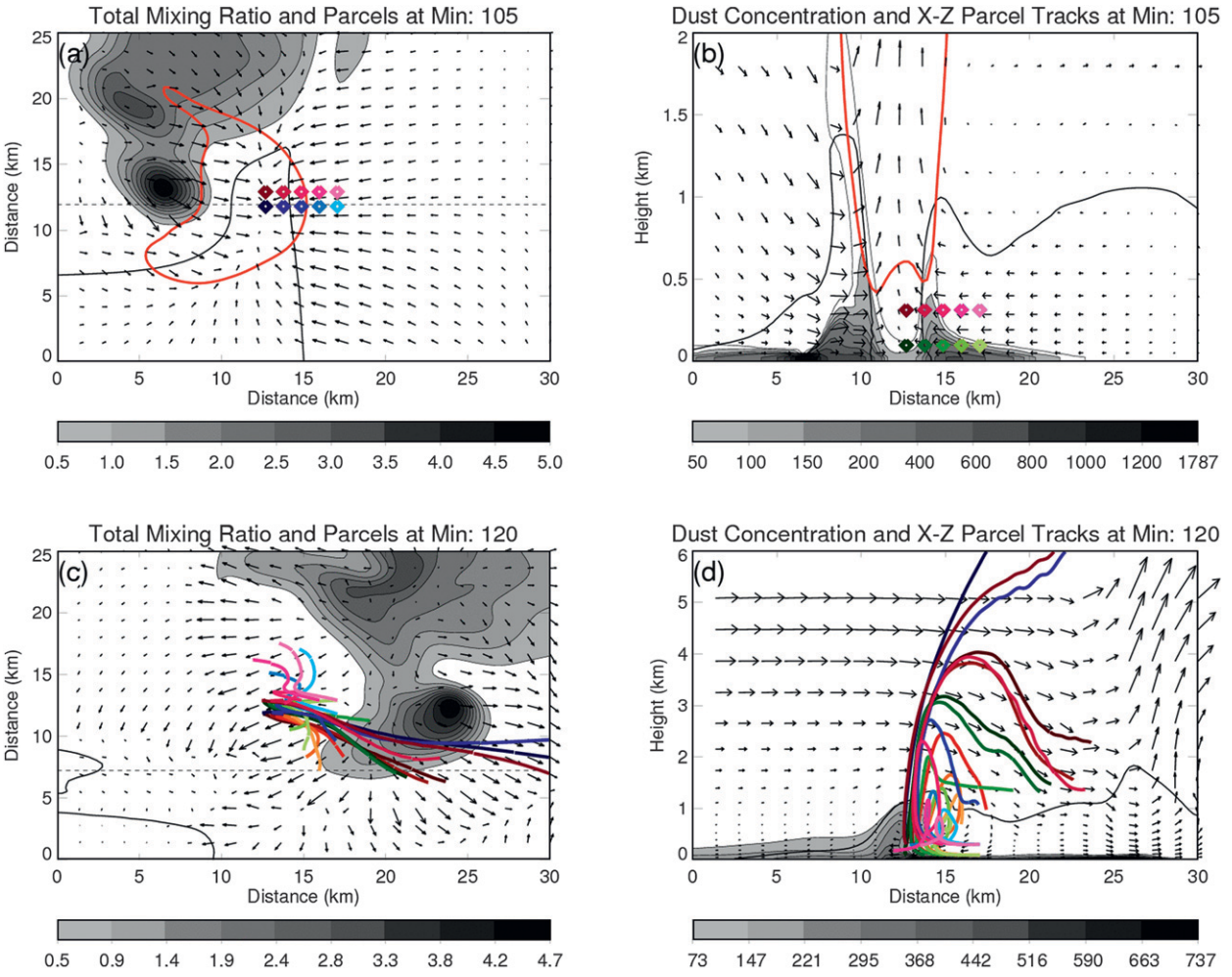

FIG. 16. EXP-BOUNDARY with parcel trajectories during the 15-min period from 105 to 120 min. Plots are as in Fig. 9.

of a convergence boundary on dust ingestion (i.e., EXP-BOUNDARY), it is seen that boundary interactions with supercells can enhance mineral dust ingestion in an initially clean environment by 1) acting as a source of background dust out ahead of the cold pool beneath the updraft and 2) enhancing the strength of the updraft and hence vertical advection as a result of the collision. These experiments show that large differences can arise in the manner in which dust is ingested by supercell storms, as well as in the concentrations of the ingested dust. This also demonstrates the necessity of an appropriate dust representation for numerical investigations.

While this study is not the first to our knowledge to directly simulate a mesoscale dust storm using a dust emission scheme, it is the first experiment that directly investigates and compares dust ingestion contributions from different production sources. Takemi (2005) simulated an idealized squall line in the Gobi Desert with 2-km grid spacing in order to study mineral dust transport from dust produced by the cold pool. He concluded that strong cold pool wind is the source of mineral dust lofting, and that turbulence at the leading edge of the cold pool acts to detrain dust out of the cold pool and into the updraft at the cold pool edge. Additionally, Tulet et al. (2010) simulated mesoscale convective systems (MCS) with a finest grid spacing of 3 km over Niger and found a similar mechanism for dust entrainment into the parent convection. The dust lofting and ingestion process found in these studies are in agreement with the EXP-STORM results shown in this paper. The amount of dust ingested relative to dust lofted in Takemi (2005) and Tulet et al. (2010) is approximately 10%, which is also exhibited here in EXP-STORM. This provides increased confidence in the kinematic mechanism of dust ingestion by storms from cold pool lofting within a clean atmosphere. However, as previously mentioned, the dust regime simulated by Takemi and

Tulet et al. (2010) of a convective complex lofting and ingesting dust within an initially clean environment is only one common regime.

As shown in this paper, deep convection propagating within an initially dusty atmosphere can dramatically enhance ingested dust concentrations, whereby the ratio of dust ingested to the largest background concentration is close to 1. In EXP-BACKGROUND the environment initially contained 1000 cm^{-3} of dust near the surface and the supercell contained ~1000 cm^{-3} in the updraft at 4 km AGL. This contribution to the storm is significantly larger than exhibited in EXP-STORM and the experiments of Takemi (2005) and Tulet et al. (2010). Such variations in the dust concentrations can significantly impact the microphysical responses of precipitation processes (van den Heever et al. 2006). Additionally, this paper has shown that nearby convergence boundaries can further complicate the method of dust ingestion by a supercell storm by providing an additional source of environmental dust.

The large differences in ingested dust concentrations among the three simulations presented in this paper demonstrate 1) how efficiently a supercell propagating within a dusty atmosphere ingests mineral dust, 2) the relative difficulty of a supercell being able to ingest its own lofted dust, 3) the role that additional surface boundaries play in enhancing dust ingestion by the parent storm, and 4) the importance of choosing an appropriate dust initialization method when simulating dust storms.

Although it is known that mineral dust acts effectively as cloud condensation nuclei and ice nuclei (Twohy et al. 2009), the mineral dust simulated in this experiment is not microphysically active. As such, the analysis presented in this paper only pertains to the ingestion pathway of dust into supercell storms and the relative amounts of dust ingested depending on the dust source. Research is currently in progress to allow dust to nucleate to form cloud droplets and ice. This will permit analysis of the microphysical implications of mineral dust ingestion within common dust regimes, along with analysis pertaining to vertical dust redistribution and radiative effects.

Acknowledgments. This work was funded by the Department of Defense Center for Geosciences/Atmospheric Research at Colorado State University under Cooperative Agreement W911NF-06-2-0015 with the Army Research Laboratory. A special thanks is given to Stephen Saleeby for assistance with the dust code, and to Clayton McGee of CSU for providing us with the parcel trajectory algorithm used in this study. The authors also thank the two anonymous reviewers, whose helpful comments improved the content of this manuscript.

REFERENCES

Albrecht, B. A., 1989: Aerosols, cloud microphysics, and fractional cloudiness. *Science,* **245,** 1227–1230.

Baron, P. A., and K. Willeke, 2001: *Aerosol Measurement: Principles, Techniques and Applications*. 2nd ed. Wiley-Interscience, 1131 pp.

Bluestein, H. B., and M. L. Weisman, 2000: The interaction of numerically simulated supercells initiated along lines. *Mon. Wea. Rev.,* **128,** 3128–3149.

Chen, W., and D. W. Fryrear, 2002: Sedimentary characteristics of a haboob dust storm. *Atmos. Res.,* **61,** 75–85.

Cotton, W. R., and Coauthors, 2003: RAMS 2001: Current status and future directions. *Meteor. Atmos. Phys.,* **82,** 5–29.

DeMott, P. J., K. Sassen, M. R. Poellet, D. Baumgardner, D. C. Rogers, S. D. Brooks, A. J. Prenni, and S. M. Kreidenweis, 2003: African dust aerosols as atmospheric ice nuclei. *Geophys. Res. Lett.,* **30,** 1732, doi:10.1029/2003GL017410.

Droegemeier, K. K., and R. B. Wilhelmson, 1985: Three-dimensional numerical modeling of convection produced by interacting thunderstorm outflows. Part I: Control simulation and low-level moisture variations. *J. Atmos. Sci.,* **42,** 2381–2403.

Fécan, F., B. Marticorena, and G. Bergametti, 1999: Parametrization of the increase of the Aeolian erosion threshold wind friction velocity due to soil moisture for arid and semi-arid areas. *Ann. Geophys.,* **17,** 149–157.

Feingold, G., W. R. Cotton, S. M. Kreidenweis, and J. T. Davis, 1999: The impact of giant cloud condensation nuclei on drizzle formation in stratocumulus: Implications for cloud radiative properties. *J. Atmos. Sci.,* **56,** 4100–4117.

Field, P. R., and Coauthors, 2006: Some ice nucleation characteristics of Asian and Saharan desert dust. *Atmos. Chem. Phys.,* **6,** 2991–3006.

Flatau, P. J., G. J. Tripoli, J. Verlinde, and W. R. Cotton, 1989: The CSU-RAMS Cloud Microphysical Module: General Theory and Code Documentation. Atmospheric Science Paper 451, Department of Atmospheric Science, Colorado State University, 88 pp.

Gillette, D. A., and R. Passi, 1988: Modeling dust emission caused by wind erosion. *J. Geophys. Res.,* **93,** 14 233–14 242.

Ginoux, P., M. Chin, I. Tegen, J. M. Prospero, B. Holden, O. Dubovik, and S.-J. Lin, 2001: Sources and distributions of dust aerosols simulated with the GOCART model. *J. Geophys. Res.,* **106,** 20 255–20 273.

Hansell, R. A., and Coauthors, 2010: An assessment of the surface longwave direct radiative effect of airborne Saharan dust during the NAMMA field campaign. *J. Atmos. Sci.,* **67,** 1048–1065.

Harrington, J. Y., 1997: The effects of radiative and microphysical processes on simulated warm and transition season Arctic stratus. Ph.D. dissertation, Atmospheric Science Paper 637, Department of Atmospheric Science, Colorado State University, 289 pp.

Hill, G. E., 1974: Factors controlling the size and spacing of cumulus clouds as revealed by numerical experiments. *J. Atmos. Sci.,* **31,** 646–673.

Houghton, J. T., Y. Ding, D. J. Griggs, M. Noguer, P. J. van der Linden, X. Dai, K. Maskell, and C. A. Johnson, Eds., 2001: *Climate Change 2001: The Scientific Basis.* Cambridge University Press, 881 pp.

Isono, K., M. Komabayasi, and A. Ono, 1959: The nature and origin of ice nuclei in the atmosphere. *J. Meteor. Soc. Japan,* **37,** 211–233.

Jensen, E., D. Starr, and B. Toon, 2004: Mission investigates tropical cirrus clouds. *Eos, Trans. Amer. Geophys. Union,* **84,** 45, doi:10.1029/2004EO050002.

Kang, J.-Y., S.-C. Yoon, Y. Shao, and S.-W. Kim, 2011: Comparison of vertical dust flux by implementing three dust emission schemes in WRF/Chem. *J. Geophys. Res.,* **116,** D09202, doi:10.1029/2010JD014649.

Khain, A. P., D. Rosenfeld, and A. Pokrovsky, 2005: Aerosol impact on the dynamics and microphysics of deep convective clouds. *Quart. J. Roy. Meteor. Soc.,* **131,** 2639–2663.

——, N. BenMoshe, and A. Pokrovsky, 2008: Factors determining the impact of aerosols on surface precipitation from clouds: An attempt at classification. *J. Atmos. Sci.,* **65,** 1721–1748.

Klemp, J. B., and R. B. Wilhelmson, 1978a: The simulation of three-dimensional convective storm dynamics. *J. Atmos. Sci.,* **35,** 1070–1096.

——, and ——, 1978b: Simulations of right- and left-moving storms produced through storm splitting. *J. Atmos. Sci.,* **35,** 1097–1110.

Knippertz, P., C. Deutscher, K. Kandler, T. Muller, O. Schulz, and L. Schultz, 2007: Dust mobilization due to density currents in the Atlas region: Observations from the SAMUM 2006 field campaign. *J. Geophys. Res.,* **112,** D21109, doi:10.1029/2007JD008774.

——, J. Trentmann, and A. Seifert, 2009: High-resolution simulations of convective pools over the northwestern Sahara. *J. Geophys. Res.,* **114,** D08110, doi:10.1029/2008JD011271.

Lawson, T. J., 1971: Haboob structure at Khartoum. *Weather,* **26,** 105–112.

Lemon, L. R., and C. A. Doswell, 1979: Severe thunderstorm evolution and mesocyclone structure as related to tornadogenesis. *Mon. Wea. Rev.,* **107,** 1184–1197.

Lerach, D. G., B. J. Gaudet, and W. R. Cotton, 2008: Idealized simulations of aerosol influences on tornadogenesis. *Geophys. Res. Lett.,* **35,** L23806, doi:10.1029/2008GL035617.

Levin, Z., E. Ganor, and V. Gladstein, 1996: The effects of desert particles coated with sulfate on rain formation in the eastern Mediterranean. *J. Appl. Meteor.,* **35,** 1511–1523.

Lewis, J. M., M. L. Kaplan, R. Vellore, R. M. Rabin, J. Hallet, and S. A. Cohn, 2010: Dust storm over the Black Rock Desert: Larger-scale dynamic signatures. *J. Geophys. Res.,* **116,** D06113, doi:10.1029/2010JD014784.

Lilly, D. K., 1962: On the numerical simulation of buoyant convection. *Tellus,* **14,** 148–172.

Liu, M., D. L. Westphal, A. L. Walker, T. R. Holt, K. A. Richardson, and S. D. Miller, 2007: COAMPS real-time dust storm forecasting during Operation Iraqi Freedom. *Wea. Forecasting,* **22,** 192–206.

Markowski, P. M., J. M. Straka, and E. N. Rasmussen, 2002: Direct surface thermodynamic observations within the rear-flank downdrafts of nontornadic and tornadic supercells. *Mon. Wea. Rev.,* **130,** 1692–1721.

——, ——, and ——, 2003: Tornadogenesis resulting from the transport circulation by a downdraft: Idealized numerical simulations. *J. Atmos. Sci.,* **60,** 795–823.

——, E. Rasmussen, J. Straka, R. Davies-Jones, Y. Richardson, and R. J. Trapp, 2008: Vortex lines within low-level mesocyclones obtained from pseudo-dual-Doppler radar observations. *Mon. Wea. Rev.,* **136,** 3513–3535.

Marsham, J. H., D. J. Parker, C. M. Grams, C. M. Taylor, and J. M. Haywood, 2008: Uplift of Saharan dust south of the intertropical discontinuity. *J. Geophys. Res.,* **113,** D21102, doi:10.1029/2008JD009844.

Marticorena, B., and G. Bergametti, 1995: Modeling the atmospheric dust cycle: 1. Design of a soil-derived dust emission scheme. *J. Geophys. Res.,* **100,** 16 415–16 430.

Matrosov, S. Y., 1999: Retrieval of vertical profiles of ice cloud microphysics from radar and IR measurements using tuned regressions between reflectivity and cloud parameters. *J. Geophys. Res.,* **104,** 16 741–16 753.

Mesinger, F., and A. Arakawa, 1976: Numerical methods used in atmospheric models. GARP Publication Series 14, WMO/ICSU Joint Organizing Committee, 64 pp.

Meyers, M. P., R. L. Walko, J. Y. Harrington, and W. R. Cotton, 1997: New RAMS cloud microphysics parameterization. Part II: The two-moment scheme. *Atmos. Res.,* **45,** 3–39.

Miller, S., A. Kuciauskas, M. Liu, Q. Ji, J. Reid, D. Breed, A. Walker, and A. Mandoos, 2008: Haboob dust storms of the southern Arabian Peninsula. *J. Geophys. Res.,* **113,** D01202, doi:10.1029/2007JD008550.

Möhler, O., and Coauthors, 2006: Efficiency of the deposition mode ice nucleation on mineral dust particles. *Atmos. Chem. Phys. Discuss.,* **6,** 1539–1577.

Perry, K., T. Cahill, R. Eldred, D. D. Dutcher, and T. E. Gill, 1997: Long-range transport of North African dust to the eastern United States. *J. Geophys. Res.,* **102,** 11 225–11 238.

Pielke, R. A., and Coauthors, 1992: A comprehensive meteorological modeling system—RAMS. *Meteor. Atmos. Phys.,* **49,** 69–91.

Prospero, J. M., 1996: Saharan dust transport over the North Atlantic Ocean and Mediterranean: An overview. *The Impact of Desert Dust across the Mediterranean,* S. Guerzoni and R. Chester, Eds., Kluwer Academic, 133–151.

——, 1999: Long-term measurements of the transport of African mineral dust to the southeastern United States: Implications for regional air quality. *J. Geophys. Res.,* **104,** 15 917–15 927.

Quijano, A. L., I. N. Sokolik, and O. B. Toon, 2000: Radiative heating rates and direct radiative forcing by mineral dust in cloudy atmospheric conditions. *J. Geophys. Res.,* **105,** 12 207–12 219.

Ramanathan, V., P. J. Crutzen, J. T. Kiehl, and D. Rosenfeld, 2001: Aerosols, climate, and the hydrologic cycle. *Science,* **294,** 2119–2124.

Reinfried, F., I. Tegen, B. Heinhold, O. Hellmuth, K. Schepanski, U. Cubasch, H. Hubener, and P. Knippertz, 2009: Simulations of convectively driven density currents in the Atlas region using a regional model: Impacts on dust emission and sensitivity to horizontal resolution and convection schemes. *J. Geophys. Res.,* **114,** D08127, doi:10.1029/2008JD010844.

Roberts, P., and J. Hallett, 1968: A laboratory study of the ice nucleating properties of some mineral particulates. *Quart. J. Roy. Meteor. Soc.,* **94,** 25–34.

Rosenfeld, D., and R. Nirel, 1996: Seeding effectiveness—The interaction of desert dust and the southern margins of rain cloud systems in Israel. *J. Appl. Meteor.,* **35,** 1502–1510.

——, Y. Rudich, and R. Lahav, 2001: Desert dust suppressing precipitation: A possible desertification feedback loop. *Proc. Natl. Acad. Sci. USA,* **98,** 5975–5980.

Saleeby, S. M., and W. R. Cotton, 2004: A large-droplet mode and prognostic number concentration of cloud droplets in the Colorado State University Regional Atmospheric Modeling System (RAMS). Part I: Module descriptions and supercell test simulations. *J. Appl. Meteor.,* **43,** 182–195.

Sassen, K., P. J. DeMott, J. M. Prospero, and M. R. Poellet, 2003: Saharan dust storms and indirect aerosol effects on clouds:

CRYSTAL-FACE results. *Geophys. Res. Lett.,* **30,** 1633, doi:10.1029/2003GL017371.

Slinn, W. G. N., 1982: Estimates for the long-range transport of air pollution. *Water Air Soil Poll.,* **18,** 45–64.

Smagorinsky, J., 1963: General circulation experiments with the primitive equations. I. The basic experiment. *Mon. Wea. Rev.,* **91,** 99–164.

Smith, M. A., 2007: Evaluation of mesoscale simulations of dust sources, sinks, and transport over the Middle East. M.S. thesis, Department of Atmospheric Science, Colorado State University, 126 pp.

Snook, N., and M. Xue, 2008: Effects of microphysical drop size distribution on tornadogenesis in supercell thunderstorms. *Geophys. Res. Lett.,* **35,** L24803, doi:10.1029/2008GL035866.

Storer, R. L., S. C. van den Heever, and G. L. Stephens, 2010: Modeling aerosol impacts on convective storms in different environments. *J. Atmos. Sci.,* **67,** 3904–3915.

Sutton, I. I., 1925: Haboobs. *Quart. J. Roy. Meteor. Soc.,* **51,** 25–50.

Takemi, T., 2005: Explicit simulations of convective-scale transport of mineral dust in severe convective weather. *J. Meteor. Soc. Japan,* **83A,** 187–203.

Tegen, I., and I. Fung, 1994: Modeling of mineral dust in the atmosphere: Sources, transport, and optical thickness. *J. Geophys. Res.,* **99,** 22 897–22 914.

Tompkins, A. M., 2001: Organization of tropical convection in low vertical wind shears: The role of cold pools. *J. Atmos. Sci.,* **58,** 1650–1672.

Tulet, P., K. Crahan-Kaku, M. Leriche, B. Aouizerats, and S. Crumeyrolle, 2010: Mixing of dust aerosols into a mesoscale convective system. Generation, filtering, and possible feedbacks on ice anvils. *Atmos. Res.,* **96,** 302–314.

Twohy, C. H., and Coauthors, 2009: Saharan dust particles nucleate droplets in eastern Atlantic clouds. *Geophys. Res. Lett.,* **36,** L01807, doi:10.1029/2008GL035846.

Twomey, S., 1977: The influence of pollution on the shortwave albedo of clouds. *J. Atmos. Sci.,* **34,** 1149–1152.

van den Heever, S. C., G. G. Carrió, W. R. Cotton, P. J. DeMott, and A. J. Prenni, 2006: Impacts of nucleating aerosol on Florida storms. Part I: Mesoscale simulations. *J. Atmos. Sci.,* **63,** 1752–1775.

——, G. L. Stephens, and N. B. Wood, 2011: Aerosol indirect effects on tropical convection characteristics under conditions of radiative–convective equilibrium. *J. Atmos. Sci.,* **68,** 699–718.

Verlinde, J., P. J. Flatau, and W. R. Cotton, 1990: Analytical solutions to the collection growth equation: Comparison with approximate methods and application to cloud microphysics parameterization schemes. *J. Atmos. Sci.,* **47,** 2871–2880.

Walko, R. L., C. J. Tremback, R. A. Pielke, and W. R. Cotton, 1995: An interactive nesting algorithm for stretched grids and variable nesting ratios. *J. Appl. Meteor.,* **34,** 994–999.

——, and Coauthors, 2000: Coupled atmosphere–biophysics–hydrology models for environmental modeling. *J. Appl. Meteor.,* **39,** 931–944.

Weisman, M. L., and J. B. Klemp, 1982: The dependence of numerically simulated convective storms on vertical wind shear and buoyancy. *Mon. Wea. Rev.,* **110,** 504–520.

——, and ——, 1984: The structure and classification of numerically simulated convective storms in directionally varying wind shears. *Mon. Wea. Rev.,* **112,** 2479–2498.

Yin, Y., S. Wurzler, Z. Levin, and T. G. Reisin, 2002: Interactions of mineral dust particles and clouds: Effects on precipitation and cloud optical properties. *J. Geophys. Res.,* **107,** 4724, doi:10.1029/2001JD001544.

Zuberi, B., A. Bertram, C. Cassa, L. Molina, and M. Molina, 2002: Heterogeneous nucleation of ice in $(NH_4)_2SO_4$-H_2O particles with mineral dust immersions. *Geophys. Res. Lett.,* **29,** 1504, doi:10.1029/2001GL014289.

Zubler, E. M., D. Folini, U. Lohmann, D. Lüthi, A. Muhlbauer, S. Pousse-Nottelmann, C. Schar, and M. Wild, 2011: Implementation and evaluation of aerosol and cloud microphysics in a regional climate model. *J. Geophys. Res.,* **116,** D02211, doi:10.1029/2010JD014572.